Testing the evolutionary link between submillimetre galaxies and quasars: CO observations of QSOs at $z \sim 2$

K. E. K. Coppin[1], A. M. Swinbank[1], R. Neri[2], P. Cox[2], D. M. Alexander[3], Ian Smail[1], M. J. Page[4], J. A. Stevens[5], K. K. Knudsen[6], R. J. Ivison[7,8], A. Beelen[9], F. Bertoldi[6], A. Omont[10]

[1] *Institute for Computational Cosmology, Durham University, South Road, Durham, DH1 3LE*
[2] *Institut de RadioAstronomie Millimétrique (IRAM), 300 rue de la Piscine, Domaine Universitaire, 38406 Saint Martin d'Hères, France*
[3] *Department of Physics, Durham University, South Road, Durham, DH1 3LE*
[4] *UCL, Mullard Space Science Laboratory, Holmbury St. Mary, Dorking, Surrey RH5 6NT*
[5] *Centre for Astrophysics Research, University of Hertfordshire, College Lane, Hatfield, AL10 9AB*
[6] *Argelander-Institut für Astronomie, University of Bonn, Auf dem Hügel 71, D-53121 Bonn, Germany*
[7] *Institute for Astronomy, University of Edinburgh, Royal Observatory, Blackford Hill, Edinburgh, EH9 3HJ*
[8] *UK Astronomy Technology Centre, Royal Observatory, Blackford Hill, Edinburgh, EH9 3HJ*
[9] *Institut d'Astrophysique Spatiale, Université Paris-Sud, F-91405 Orsay, France*
[10] *Institut d'Astrophysique de Paris, Université Pierre & Marie Curie, 98 bis Boulevard Arago, F-75014 Paris, France*

8 July 2008

ABSTRACT

We have used the IRAM Plateau de Bure millimeter interferometer and the UKIRT 1–5 μm Imager Spectrometer (UIST) to test the connection between the major phases of spheroid growth and nuclear accretion by mapping CO emission in nine submillimetre-detected QSOs at $z = 1.7$–2.6 with black hole (BH) masses derived from near-infrared spectroscopy. When combined with one QSO obtained from the literature, we present sensitive CO(3–2) or CO(2–1) observations of 10 submillimetre-detected QSOs selected at the epoch of peak activity in both QSOs and submillimetre (submm) galaxies (SMGs). CO is detected in 5/6 very optically luminous ($M_B \sim -28$) submm-detected QSOs with BH masses $M_{BH} \simeq 10^9$–10^{10} M$_\odot$, confirming the presence of large gas reservoirs of $M_{gas} \simeq 3.4 \times 10^{10}$ M$_\odot$. Our BH masses and dynamical mass constraints on the host spheroids suggest, at face value, that these optically luminous QSOs at $z = 2$ lie about an order of magnitude above the local BH-spheroid relation, M_{BH}/M_{sph}, although this result is dependent on the size and inclination of the CO-emitting region. However, we find that their BH masses are ~ 30 times too large and their surface density is ~ 300 times too small to be related to typical SMGs in an evolutionary sequence. Conversely, we measure weaker CO emission in four fainter ($M_B \sim -25$) submm-detected QSOs with properties, BH masses ($M_{BH} \simeq 5 \times 10^8$ M$_\odot$), and surface densities similar to SMGs. These QSOs appear to lie near the local M_{BH}/M_{sph} relation, making them plausible 'transition objects' in the proposed evolutionary sequence linking QSOs to the formation of massive young galaxies and BHs at high-redshift. We show that SMGs have a higher incidence of bimodal CO line profiles than seen in our QSO sample, which we interpret as an effect of their relative inclinations, with the QSOs seen more face-on. Finally, we find that the gas masses of the four fainter submm-detected QSOs imply that their star formation episodes could be sustained for ~ 10 Myr, and are consistent with representing a phase in the formation of massive galaxies which overlaps a preceding SMG starburst phase, before subsequently evolving into a population of present-day massive ellipticals.

Key words: galaxies: high-redshift – galaxies: evolution – galaxies: formation – galaxies: kinematics and dynamics – quasars: emission lines – submillimetre

1   INTRODUCTION

It has been established that every massive, local spheroid harbours a supermassive black hole (SMBH) in its centre whose mass is proportional to that of its host (e.g. Magorrian et al. 1998; Gebhardt et al. 2000). This suggests that the black holes (BHs) and their surrounding galaxies were formed synchronously. This hypothesis has found support from hydrodynamical simulations of galaxy formation, which use feedback from winds and outflows from active galactic nuclei (AGN) to link the growth of the SMBH to that of its host (e.g. Di Matteo, Springel & Hernquist 2005; Hopkins et al. 2005; Bower et al. 2006). Thus these models support a picture, first presented by Sanders et al. (1988), where a starburst-dominated ultra-luminous infrared galaxy (ULIRG), arising from a merger, evolves first into an obscured QSO and then into an unobscured QSO, before finally becoming a passive spheroid.

The high-redshift population of ULIRGs in this proposed evolutionary cycle are the submillimetre (submm) galaxies (SMGs; Smail, Ivison & Blain 1997; Chapman et al. 2005; Coppin et al. 2006). These systems have ULIRG-like bolometric luminosities, $L_{IR} \geq 10^{12} L_{\odot}$ (Kovács et al. 2006; Coppin et al. 2008), and they have many of the properties expected for gas-rich mergers (Swinbank et al. 2004, 2006; Tacconi et al. 2006). This population evolves rapidly out to a peak at $z \sim 2.3$, crudely matching the evolution of QSOs (Chapman et al. 2005) and providing additional circumstantial evidence for a link between SMBH growth and spheroids. Two further results have shed light on the evolutionary link between SMGs and QSOs. Firstly, a modest fraction of optically luminous QSOs at $z \sim 2$ are detected in the submm/mm ($\sim (25 \pm 10)\%$; Omont et al. 2003) showing that the QSO- and SMG-phases do not overlap significantly, given the lifetime estimates of the two populations (QSOs make up $\sim 4\%$ of flux-limited samples of SMGs; Chapman et al. 2005). But when a QSO *is* detected in the submm/mm then it could to be in the transition phase from an SMG to an unobscured QSO, making its properties a powerful probe of the evolutionary cycle (e.g. Stevens et al. 2005; Page et al. 2004). Secondly, the evolutionary state of the SMBHs within SMGs can also be judged using the 2-Ms *Chandra* Deep Field North observations (Alexander et al. 2003) to derive accurate AGN luminosities and hence lower limits on the BH masses (M_{BH}) in those SMGs with precise redshifts in this region (Alexander et al. 2005a,b; Borys et al. 2005). These studies suggest that the AGN in typical SMGs are growing almost continuously – but that the SMBHs in these galaxies appear to be several times less massive than seen in comparably massive galaxies at $z \sim 0$ (Alexander et al. 2008).

Together these results argue for a fast transition from a star-formation-dominated SMG-phase to the AGN-dominated QSO-phase (Page et al. 2004). The latter phase will result in the rapid BH growth necessary to account for the present-day relation between spheroid and SMBH masses (e.g. Magorrian et al. 1998; Gebhardt et al. 2000). *Can we confirm this and more generally test the proposed evolutionary link between SMGs and QSOs at the peak of their activity at $z \sim 2$?*

This evolutionary cycle has been tested in the local Uni-verse by comparing the properties of QSOs and ULIRGs (e.g. Tacconi et al. 2002). However, both of these populations are $1000\times$ less abundant in the local Universe than they were at the era of their peak activity at $z \sim 2$ and so we have to be cautious about extrapolating from local examples to the high-redshift progenitors of the bulk of today's massive spheroids (Genzel et al. 2003; Swinbank et al. 2006). Thus, to properly test the validity of this cycle for typical spheroids we have to compare QSOs and ULIRGs at the era where their populations peaked: $z \sim 2$.

The critical pieces of information needed to test the link between SMGs and QSOs are the relative dynamical, gas and SMBH masses of these two populations. In principle the dynamical masses can be derived from optical or near-infrared observations of emission line gas in the SMGs or QSOs (see Swinbank et al. 2004, 2005, 2006). However, there is the problem of removing the QSO emission in these observations, as well as the effects of dust obscuration and outflows. In contrast, molecular CO emission line profiles are relatively immune to the effects of obscuration and outflows, while at the same time yielding additional constraints on the relationship between QSOs and SMGs from their gas masses.

There is currently a lack of sensitive CO observations of QSOs at $z \sim 1$–3, with data published on only eight sources (e.g. Frayer et al. 1998; Guilloteau et al. 1999; Beelen et al. 2004; Hainline et al. 2004). Instead the focus has been on CO studies of QSOs at $z \gtrsim 4$ (e.g. Omont et al. 1996; Walter et al. 2004; Riechers et al. 2006), although these QSOs have little overlap with the redshift range where SMGs are typically detected. The paucity of CO constraints for $z > 1$ QSOs also reflects the difficulty in determining their systemic redshifts with sufficient precision to guarantee that the CO emission falls within the bandwidth of typical millimetre (mm) correlators. However, sensitive near-infrared spectroscopy of the C IV, Mg II, and [O III]5007 emission lines in QSOs can provide redshifts with required precision as well as Hα or Hβ fluxes and line widths to yield M_{BH} estimates (Takata et al. 2006; Alexander et al. 2008).

We have carried out a quantitative test of the proposed link between SMGs and QSOs at $z \sim 2$ where both populations are most common. We have obtained precise systemic redshifts from near-infrared spectroscopy of potential transition QSOs (i.e. submm/mm-detected QSOs) and then used the IRAM Plateau de Bure Interferometer (PdBI) to search for CO emission. We relate their dynamical, gas and SMBH masses to SMGs from the PdBI CO survey (Greve et al. 2005). We test: a) whether the cold gas masses in these QSOs are similar to those in SMGs; b) whether the line widths and dynamical masses of these two populations are comparable; and c) how the ratio of SMBH to dynamical masses for these submm-detected QSOs relate to the estimates for SMGs and those for optically luminous QSOs (which lie on the present-day M_{BH}–M_{σ} relation; McLure & Dunlop 2004). Together these observations can constrain the proposed evolutionary sequence which links QSOs to the formation of massive young galaxies and SMBHs at high redshift.

We describe the sample selection, observations and data reduction in §2. The results of the near-infrared and mm CO spectra are given in §3. The CO properties of the submm-detected QSOs are compared and contrasted with SMGs in §4, and we discuss the evolutionary status of the
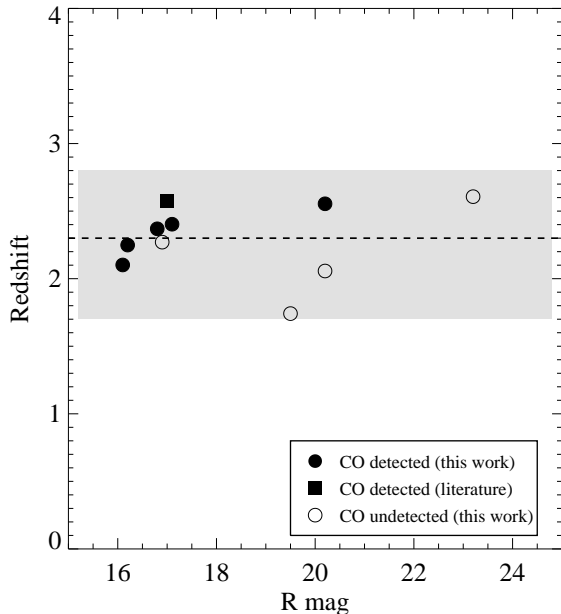
Figure 1. *R*-band apparent magnitude versus redshift for our sample of submm-detected QSOs. We show that these lie within the interquartile range (shaded region) of the redshift distribution of SMGs (median $<z>\simeq 2.3$; dashed line) from Chapman et al. (2005). This shows that we are probing a wide range in optical luminosities (and potentially a wide range in $M_{\rm BH}$) at the epoch where the QSO and SMG populations peak.

submm-detected QSOs in §5. Our conclusions are given in §6. We adopt cosmological parameters from the *WMAP* fits in Spergel et al. (2003): $\Omega_{\Lambda} = 0.73$, $\Omega_{\rm m} = 0.27$, and $H_0 = 71\,{\rm km\,s^{-1}\,Mpc^{-1}}$. All quoted magnitudes are on the Vega system.

2   OBSERVATIONS, REDUCTION AND REDSHIFTS

2.1   Sample Selection

The objective of this study is to test the link between SMGs and QSOs at the era where these populations peaked. We have therefore selected radio-quiet QSOs with a redshift distribution matched to SMGs ($\langle z \rangle \sim 2.3$, Chapman et al. 2005) and with $850\,\mu$m fluxes $\gtrsim 5$ mJy. The $S_{850\,\mu\rm m} \gtrsim 5$ mJy flux limit selects comparatively bright QSOs and SMGs and is imposed so that the sources would be sufficiently bright to be detected in CO. We choose submm-detected QSOs from three main samples: we select five QSOs from a submm photometry survey of optically-bright QSOs by Omont et al. (2003) – HS1002+4400, J140955.5+562827, J154359.3+535903, HS1611+4719, and J164914.9+530316, we select two QSOs from the submm photometry survey of X-ray absorbed QSOs by Stevens et al. (2005) – RXJ121803.82+470854.6 and RXJ124913.86–055906.2, and finally we include two QSOs found in blank-field submm surveys by Chapman et al. (2005) and Greve et al. (2004), SMM J131222.35+423814.1 and MM J163655+4059, respectively, and SMM J123716.01+620323.3, an optically-

selected QSO targetted in submm photometry mode by Chapman et al. (2005).

The final sample comprises 10 submm-detected QSOs with similar fluxes to the SMG sample (Greve et al. 2005; $\gtrsim 5$ mJy at $850\,\mu$m, assuming $850\,\mu$m/1.2 mm colours typical of SMGs; Greve et al. 2004), with a median of 10 mJy. The SEDs of these QSOs demonstrate that the bulk of the mm/submm luminosity arises from dust emission and is very likely associated with star formation, rather than an AGN (Beelen et al. 2006; Omont et al. 2003). Our sample spans six orders of magnitude in QSO *R*-band brightness, enabling us to potentially trace how CO properties depend on QSO luminosity or $M_{\rm BH}$ (see Fig. 1).

2.2   Near-Infrared Spectroscopy

The QSOs in this sample were spectroscopically identified through rest-frame UV spectroscopy. However, since the rest-frame UV emission lines can be extremely broad (FWHM$\sim 5000\,{\rm km\,s^{-1}}$), and can be offset in velocity with respect to the systemic redshift, precise systemic redshifts are required to ensure the CO emission falls within the PdBI receiver bandwidth. To obtain precise systemic redshifts for our targets we use the nebular emission lines of [O III]$\lambda 5007$ and Hβ which are redshifted to near-infrared wavelengths.

Seven of our submm-detected QSOs were observed with the United Kingdom InfraRed Telescope (UKIRT) 1–5$\,\mu$m Imager Spectrometer (UIST; Howatt et al. 2004). We used the *HK* grism which provides a spectral resolution of $\lambda/\Delta\lambda \sim 1000$ and covers a wavelength range 1.4–2.4μm, thus allowing us to cover Hβ, [O III]$\lambda 4959,5007$ and Hα simultaneously for most of our QSOs. The QSOs were observed between 2006 Feb and 2006 Oct. All observations were taken in $\lesssim 0.8''$ seeing and clear conditions, and were carried out using the standard ABBA configuration where the QSO was nodded by 6–12$''$ along the slit to achieve sky subtraction. Individual exposures were 240 s and the total integration times varied between 1.2 ks and 4.8 ks depending on the *K*-band magnitude of the QSO (see Table 1). In addition, three QSOs in our sample have suitable archival spectroscopy from Takata et al. (2006) and Swinbank et al. (2004, 2006).

The relevant ORAC-DR pipeline (Cavanagh et al. 2003) was used to sky-subtract, extract, wavelength calibrate, flat-field and flux calibrate the data (and in the case of integral field unit observations, forms the datacube). Spectra for the QSOs in our sample are shown in Fig. 2. To derive systemic redshifts, we simultaneously fit the Hβ and [O III]$\lambda 4959,5007$ emission lines with Gaussian profiles. The emission line flux ratio of the [O III]$\lambda 4959,5007$ emission lines is fixed such that I_{4959}/I_{5007}=2.9, and the [O III]$\lambda 4959,5007$ line widths are assumed to be the same. The fit assumes a linear continuum plus Gaussian emission line profiles allowing the velocity centroid, flux and width of the Hβ line profile to be different from [O III]. This makes a total of seven parameters to be fitted. We also derive emission line fluxes and widths for the Hα emission line (which are important for deriving $M_{\rm BH}$ using the method of Greene & Ho 2005) in a similar manner, fitting a single Gaussian emission line profile superimposed on a linear continuum. The resulting redshifts and fluxes are given in Table 2. These redshifts were subsequently used to target the CO emission with PdBI (see §2.3).

Table 1. Summary of the new near-infrared spectroscopy and mm-wave PdBI CO observations of submm-detected $2 < z < 3$ QSOs, including nine new CO observations and one published object from Beelen et al. (2004). The CO $t_{\rm exp}$ corresponds to the on-source integration time with the equivalent of a 6-element array.

Source	Near-IR Observations		CO Observations[a]				
	Date(s)	$t_{\rm exp}$ (ks)	Dates	$t_{\rm exp}$ (hrs)	Noise per channel[f] (mJy beam^{-1})	Beam FWHM	Detected?
HS1002+4400	2006 Mar 08[b]	1.8	2006 Sep 16,17,19,21,22	7.2	1.4	$4.6'' \times 3.3''$	Y
RXJ121803.82+470854.6	–	–	2001 Dec 20, 22, 24	9.0	1.2	$6.7'' \times 3.2''$	N
SMM J123716.01+620323.3	2005 Feb 16[d]	4.0	2007 May 12,18,30, Jun 3,5,18	16.0	0.5	$4.7'' \times 4.1''$	N
RXJ124913.86–055906.2	2006 Feb 25[b]	4.8	2001 Aug 5, 2002 Apr 13,14,25, May 6	9.4	1.8	$8.8'' \times 6.6''$	Y
SMM J131222.35+423814.1	2004 Jun 25[d]	2.0	2007 Jun 2,4,9,10,22,23	9.3	0.5	$5.2'' \times 4.1''$	Y
J140955.5+562827	2006 Mar 06[b]	1.2	2002 May, June, 2003 Jan-Mar[e]	37.0	0.6	$2.4'' \times 1.7''$	Y
J154359.3+535903	2006 Feb 25[b]	4.8	2006 Jun 4,5,9,11,19,26	12.1	1.2	$5.6'' \times 3.5''$	Y
HS1611+4719	2006 Aug 17[b]	3.6	2006 Jun 19,21,27, Jul 7	6.3	2.1	$5.0'' \times 4.1''$	Y
MM J163655+4059	2003 Aug 03[c], 2004 Apr 07[d]	2.4	2007 Apr 30, May 21	9.5	0.4	$5.3'' \times 4.4''$	N
J164914.9+530316	2006 Mar 06[b]	1.8	2006 Jul 20,23, Aug 15,18	6.5	1.6	$5.5'' \times 3.7''$	N

Notes:
(a) All observed in the CO(3–2) transition, except for RXJ121803.82+470854.6 observed in CO(2–1)
(b) From UIST spectroscopy (this work)
(c) From Swinbank et al. (2004)
(d) From Takata et al. (2006) and Alexander et al. (2008)
(e) From Beelen et al. (2004)
(f) With a channel width of 20 MHz

Due to the very weak [OIII]$\lambda 5007$ emission in RXJ124913.86, it was very difficult to measure a reliable redshift for the CO observations, and thus a range of possible redshifts were covered on this QSO ($z \sim 2.24$–2.26).

During the course of assembling the data for this project, we obtained a CO detection of HS1611 after securing a systemic redshift from identification of [OIII] with UIST. The positional centroid of the CO was offset by ~ 1.3 arcsec north of the optical and near-infrared QSO position, possibly indicating a companion, and HS1611 was re-observed with the UIST integral field unit (IFU) for a total of 3.6 ks on 2006 Sep 01. The UIST IFU uses an image slicer to take a $3.3'' \times 6.0''$ field and divides it into 14 slices of width $0.24''$. The dispersed spectra from the slices are reformatted on the detector to provide two-dimensional spectro-imaging, in our case also using the HK grism. We reduced the data using the relevant ORAC-DR pipeline which extracts, flatfields, wavelength calibrates the data and forms the datacube. We discuss these data in §3.1.8.

2.3 Millimetre Interferometry

We surveyed seven QSOs for CO emission using IRAM PdBI between 2006 June to 2007 June and two QSOs between 2001 December and 2002 April in conditions with good atmospheric phase stability and reasonable transparency. The observations were carried out using 3, 4, 5, and 6 antennae in the D configuration, giving a total of 3, 6, 10, and 15 baselines, respectively. For uniformity with the previous observations observations of SMGs, which will comprise our comparison sample, we have aimed to achieve the same 1-σ sensitivity as for the SMG survey (Greve et al. 2005) for the new CO observations of our sample of submm-detected QSOs: $S_{\rm CO}\,\Delta v \sim 0.3\,{\rm Jy\,km\,s^{-1}}$. We also include results on a single QSO from the literature, J140955.5 from Beelen et al. (2004), to yield a final sample of 10 QSOs. The PdBI observations are summarised in Table 1.

For data taken prior to 2007 January, the spectral correlator was adjusted to detect the line with a frequency resolu-

tion of 2.5 MHz at a bandwidth of 580 MHz. For data taken after January 2007, the spectral correlator was adjusted to detect the line with a frequency resolution of 2.5 MHz in the 1 GHz band of the new generation receivers. The visibilities were resampled to a frequency resolution of 5 MHz.

The data were calibrated, mapped and analyzed in the IRAM GILDAS[1] software package (Guilloteau & Lucas 2000). Anomalous and high phase-noise visibilities were flagged. Passband calibrations were typically made using a nearby bright quasar. Phase and amplitude calibration within each observation were calibrated using frequent observations of nearby quasars approximately every 20 min. The flux calibration was done using standard calibrators, including 3C 273, MWC 349, 1637+574, 1749+096, 0923+392, 1243-072, and CRL618, for example. We estimate a conservative error on the flux calibration of 10–15%.

For each QSO the central observing frequency of the 3.1 mm band receiver was tuned to either the redshifted CO(3–2) or CO(2–1) rotational transition, depending on the systemic near-infrared redshift derived from our spectroscopy given in Table 2. In the case of RXJ124913.86, the uncertainty on the redshift was large enough that we performed two separate observations with different central frequency tunings of 106.160 and 106.720 GHz to ensure that the CO(3–2) line was covered. We have combined these data to cover more effective bandwidth and have centered the resulting spectrum at the mean central observed frequency, 106.435 GHz, corresponding to CO(3–2) redshifted to $z \simeq 2.2487$.

Naturally weighted datacubes were made and inspected for line emission close to the QSO position. Fig. 3 shows the velocity-integrated mm emission maps over the line in each field. In Fig. 4, we show the spectra of the CO emission in the brightest pixel of the central source in each velocity-integrated mm emission map, centered on the systemic redshift of each system. We have included the maps and spec-
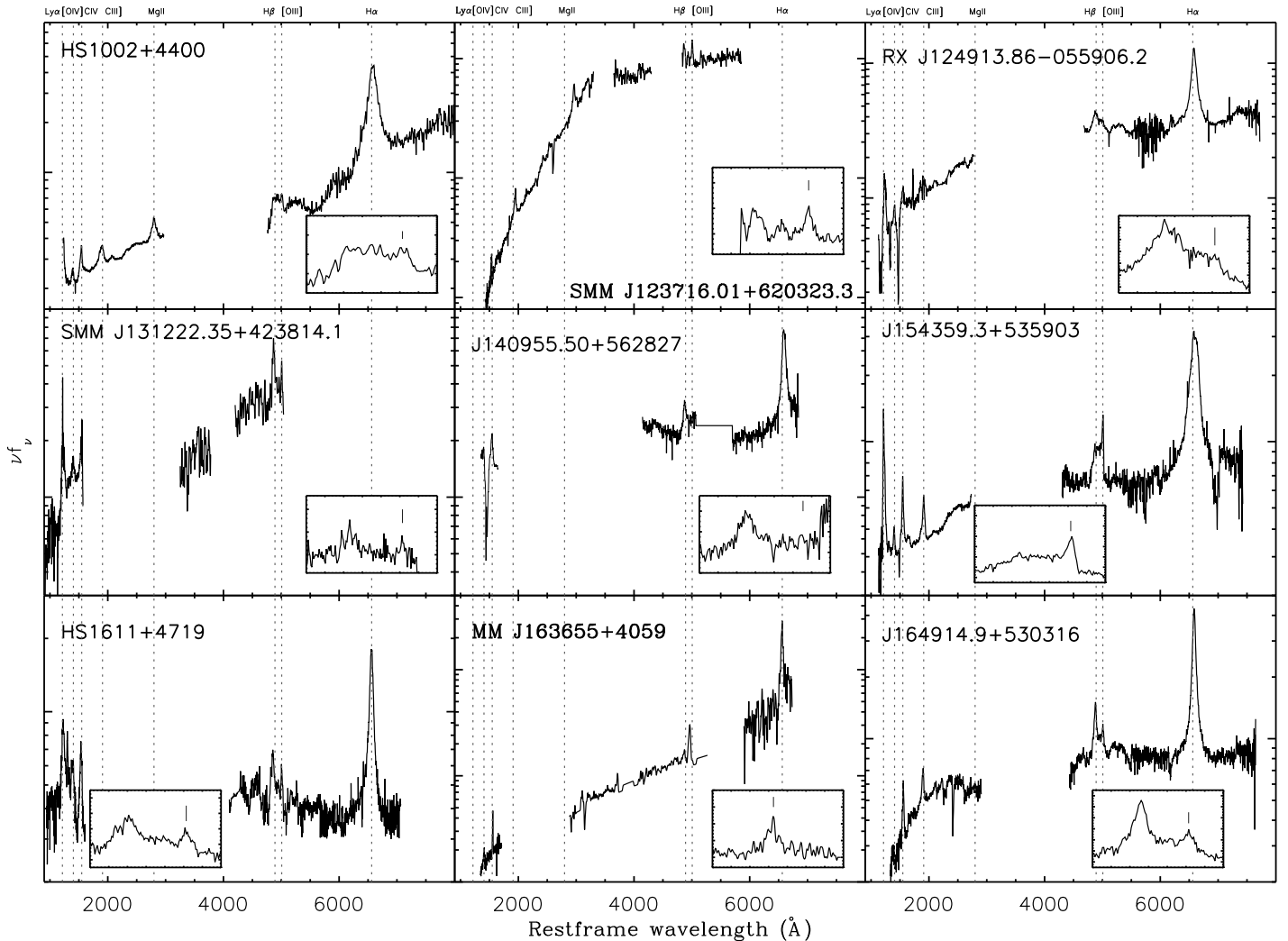
Figure 2. Restframe UV–near-infrared spectra for our sample of submm-detected QSOs. The insets show the region around the Hβ and [O III]λ5007 emission lines (all insets cover the wavelength range 4675–5100Å), except in the case of J163655, and the redshifts derived from the [O III]λ5007 emission are indicated. The redshift for J163655 was taken from the redshifted Hα due to ambiguity in the [O III]λ5007 emission lying near the edge of the wavelength coverage of the spectrograph; the inset therefore shows the region around Hα. The region around 5100–5500Å in J1409 has been masked due to strong atmospheric absorption.

tra of non-detections and in the latter cases we show the maps averaged over the central $500 \, \mathrm{km \, s^{-1}}$ of the spectra (the average line width of our sample) and spectra extracted at the phase tracking centre (or at the continuum peak for J164914.9). In all cases, we ignore the small correction for the primary beam attenuation, given that the detected sources are all close to the phase centres of the maps.

3 ANALYSIS AND RESULTS

3.1 CO properties

We present new CO data for nine QSOs, including five new CO detections. Four of our QSOs have CO detections with S/N $\gtrsim 5$, and an additional QSO is marginally detected in CO with S/N $\simeq 2.5$ with emission coincident with the phase centre (see Fig. 4). None of the QSOs appear to be resolved with the $\simeq 6$ arcsec beams ($\sim 50 \, \mathrm{kpc}$ FWHM). We include

a previous CO detection reported by Beelen et al. (2004) in our sample of submm-detected QSOs. In total therefore this gives six detections in our sample of 10 QSOs, yielding a detection rate comparable to that for SMGs by Greve et al. (2005) of $\sim 60\%$.

Looking at the non-detections, it is unlikely that the cause of the failure to detect CO emission in these four QSOs is due to the systemic redshifts being wrong, as the quality of the optical/near-infrared spectral data for these is high and similar to the successful detections (see Fig. 2). Similarly, it is unlikely that the velocity offset of the CO emission and the systemic redshift are larger than the correlator coverage (the rms deviation of z_{NIR} and z_{CO} for our CO-detected QSOs is 0.0046), since only a few systems detected at high-redshift so far show larger offsets (e.g. Hainline et al. 2004). It is also unlikely that the CO line widths are $\gg 1000 \, \mathrm{km \, s^{-1}}$ since our typical detected lines are $\lesssim 550 \, \mathrm{km \, s^{-1}}$ which is much less than the correlator bandwidth. Although extreme

CO line widths could be one reason for some of the non-detections, the most likely reason appears to be that the QSOs are simply too faint in CO to be detected given the depth of our observations. However, the non-detections do still provide useful upper limits on the CO luminosity and gas masses and therefore we include them in our analysis.

Other than one QSO (J164914.9; §3.1.10), we do not detect the continuum at 3.1 mm in any of the QSOs. This is consistent with the measured submm/mm fluxes and grey-body dust emission with a spectral form $S_\nu \propto \nu^{2+\beta}$ in the Rayleigh-Jeans regime of the spectral energy distribution with a dust emissivity $\beta = 1.5$.

The luminosity, velocity width and spatial extent of the CO line emission can be used to place limits on the gas and dynamical mass of each system. For each CO-detected QSO a Gaussian profile is fit to either 20- or 30-MHz binned data by minimising the χ^2 statistic. The 1σ errors on the best-fitting parameters are quoted where appropriate. To calculate the velocity-integrated flux density of the CO emission, we integrate the best-fitting Gaussian profile (note that we do not fit the line and continuum simultaneously). The error on the velocity-integrated flux density is calculated by boot-strapping from a Normal distribution centered on the best fitting amplitude above, with a width given by the 1σ error in the fitted amplitude, while holding the FWHM and central velocity of the best-fitting Gaussian profile fixed. The noise in the averaged channel maps, constructed from the average emission over the full width at zero intensity (FWZI) in each QSO, is determined by summing over the weights and takes into account the phase noise visibilities.

For the non-detections we calculate 3σ upper limits $S_{\rm CO} = 3\sigma (\delta v \, \Delta v_{\rm FWHM})^{1/2}$, where σ is the channel-to-channel rms noise, δv is the velocity resolution and $\Delta v_{\rm FWHM}$ is the line width (see e.g. Greve et al. 2005; Seaquist, Ivison & Hall 1995). We use the channel-to-channel rms noise of the spectra binned to a resolution of 100 MHz and adopt a line width of 500 km s^{-1}. Since our detections have typical line widths $\lesssim 550$km s^{-1}, this is a conservative assumption. In addition, this line width assumption facilitates the direct comparison of our non-detections with those of SMGs in Greve et al. (2005).

We have summarised the line properties of each source (the CO position, $z_{\rm CO}$, $L'_{\rm CO(3-2)}$ and FWHM) in Tables 3 and 4. Offsets of the CO emission from the radio position are given in Table 3, assuming that the source is unresolved using equation B2 in Ivison et al. (2007), and are less than 2σ significant in most cases. We note that we discover serendipitous $\gtrsim 4\sigma$ sources in two of the fields surveyed which may be associated with gas-rich companions to the QSOs (SMM J123716.01 and SMM J131222.35). Overdensities of submm sources have already been found by Stevens et al. (2004) around similar QSOs on slightly bigger scales than those probed here. We now discuss the CO properties of each QSO detection and non-detection in detail, as well as any serendipitous detections.

3.1.1 HS1002+4400

The integrated CO emission in this QSO is detected at $\simeq 6\sigma$, 0.8″ north of the Sloan Digital Sky Survey (SDSS; Fan et al. 1999) position (see Fig. 3). The CO(3–2) spectrum of HS1002+4400 has been binned to a frequency res-

olution of 20 MHz (54 km s^{-1}) and is shown in Fig. 4. The CO emission line is well fitted by a Gaussian profile with a FWHM of 640±160 km s^{-1}, a velocity-integrated flux density of $S_{\rm CO(3-2)} = 1.7 \pm 0.3$ Jy km s^{-1}, and a CO redshift of $z_{\rm CO} = 2.1015 \pm 0.0007$, offset by 20 ± 65 km s^{-1} from the near-infrared systemic redshift. No significant continuum emission is detected from the line-free region down to a 1-σ limit of 0.4 mJy.

3.1.2 RXJ121803.82+470854.6

Neither CO(2–1) emission at the systemic redshift nor continuum emission are seen in the map near the QSO position. To calculate a 3σ upper limit to the velocity-integrated CO(2–1) line flux of RXJ121803.82, we extract a spectrum at the QSO position (Table 2) and rebin the spectrum to a frequency resolution of 100 MHz (360 km s^{-1}), resulting in a channel rms of 0.5 mJy, and so derive an upper limit of 0.6 Jy km s^{-1}, assuming a line width of 500 km s^{-1}, centred on the $z_{\rm NIR} = 1.7416$. No significant continuum emission is detected down to a 1-σ limit of 0.2 mJy.

We do find two $\simeq 4\sigma$ serendipitous detections in the datacube, offset in velocity from the central frequency tuning, and approximately 10-20 arcsec away from the phase centre. Neither show strong broad line detections in the spectra extracted at the peak locations, so we believe these are unlikely to be true sources.

3.1.3 SMM J123716.01+620323.3

Neither CO(3–2) emission nor continuum emission are seen in the datacube near the QSO position. To calculate a 3σ upper limit to the velocity-integrated CO(3–2) line flux, we extract a spectrum at the radio position (Table 2) and rebin the spectrum to a frequency resolution of 100 MHz (270 km s^{-1}), resulting in a channel rms of 0.2 mJy, giving an upper limit of 0.3 Jy km s^{-1}, assuming a line width of 500 km s^{-1} at the systemic redshift from [OIII]λ5007 (Table 2). No significant continuum emission is detected down to a 1-σ limit of 0.2 mJy.

We find a $\simeq 4\sigma$ detection in the datacube, offset in velocity from the central frequency tuning and approximately 18 arcsec^2 south of the nominal pointing position at 12 37 15.36, 62 03 06.5 (J2000), indicating a redshift of $z_{\rm CO} = 2.0597 \pm 0.0001$, which is close to the QSO $z_{\rm NIR}$, suggesting it may be a gas-rich companion of the QSO with a separation of 170 kpc. See Fig. 5. This position corresponds to within 0.5 arcsec of an $I = 24.7$ counterpart (Smail et al. 2004) with a radio flux of $\leq 15\,\mu$Jy (Biggs & Ivison 2006) which is also undetected in the *Chandra* observations (Alexander et al. 2003). The CO line has an integrated flux of $S_{\rm CO(3-2)} = 0.2 \pm 0.06$ Jy km s^{-1} and is very narrow (FWHM=100 ± 30 km s^{-1}).

---

[2] Note that the map noise at this distance from the phase centre is only slightly degraded since the primary half power beam width (HPBW) at this frequency is $\simeq 45$ arcsec.

Table 2. Summary of the near-infrared observed properties of the submm-detected QSOs.

Source	Near-IR position (J2000) R.A.	Dec.	R	K (Vega)	$z_{\rm NIR}^a$	$\mathrm{FWHM_{H\alpha}}$ $(\mathrm{km\,s^{-1}})$	$S_{\mathrm{H\alpha}}$ $(\times 10^{-19}\,\mathrm{W/m^2})$	$\mathrm{FWHM_{[OIII]}}$ $(\mathrm{km\,s^{-1}})$
HS1002+4400	10 05 17.43	43 46 09.3	16.1	14.2	2.1015 ± 0.0010	10000 ± 1000	750 ± 100	1500 ± 300
RXJ121803.82+470854.6	12 18 04.54	47 08 51.0	19.5	17.0	1.7416	–	–	–
SMM J123716.01+620323.3	12 37 16.00	62 03 23.4	20.2	15.6	2.0568 ± 0.0013	2100 ± 500^b	48 ± 10^b	1100 ± 200
RXJ124913.86–055906.2	12 49 13.85	−05 59 19.4	16.2	13.5	2.2400 ± 0.0100	4820 ± 200	1000 ± 100	700 ± 300
SMM J131222.35+423814.1	13 12 22.32	42 38 13.9	20.2	18.0	2.5543 ± 0.0010	2600 ± 1000^b	60 ± 10^b	670 ± 300
J140955.5+562827	14 09 55.50	56 28 27.0	17.0	14.9	2.5758 ± 0.0050	4250 ± 200	220 ± 20	600 ± 200
J154359.3+535903	15 43 59.44	53 59 03.2	16.8	14.3	2.3692 ± 0.0015	8280 ± 300	770 ± 50	1000 ± 200
HS1611+4719	16 12 39.90	47 11 57.0	17.1	15.1	2.4030 ± 0.0008	4010 ± 300	300 ± 20	1000 ± 300
MM J163655+4059	16 36 55.79	40 59 10.5	23.2	19.1	2.6070 ± 0.0006	3000 ± 400	16 ± 2	1840 ± 400
J164914.9+530316	16 49 14.90	53 03 16.0	16.9	14.2	2.2704 ± 0.0009	3100 ± 300	580 ± 50	1000 ± 200

Notes:
(a) All redshifts are derived from [OIII], except for RXJ121803.82, where the redshift is derived from CIV, CIII] and MgII by Page et al. (2001) using WHT data
(b) Hα flux is calculated from the Hβ flux, assuming an intrinsic $S_{\mathrm{H\alpha}}/S_{\mathrm{H\beta}} \simeq 3.1$ (Alexander et al. 2008), and the given line width is for Hβ

Table 3. Summary of the mm and CO observed properties of the submm-detected QSOs.

Source	CO position (J2000) RA	Dec.	Offset (arcsec)	Resolution^g (kpc)	$z_{\rm CO}^h$	$S_{\rm CO}\,\Delta v^h$ $(\mathrm{Jy\,km\,s^{-1}})$	$\mathrm{FWHM_{CO}^h}$ $(\mathrm{km\,s^{-1}})$	850 μm flux (mJy)	1.2 mm flux (mJy)
HS1002+4400	10 05 17.43	43 46 10.1	0.5	33	2.1015 ± 0.0007	1.7 ± 0.3	640 ± 160	–	4.2 ± 0.8^a
RXJ121803.82+470854.6	–	–	–	42	–	≤ 0.6	–	6.8 ± 1.2^b	–
SMM J123716.01+620323.3	–	–	–	37	–	≤ 0.3	–	5.3 ± 1.7^c	–
RXJ124913.86–055906.2	12 49 13.91	−05 59 20.1	0.6	125	2.2470 ± 0.0016	1.3 ± 0.4	1090 ± 340	7.2 ± 1.4^b	–
SMM J131222.35+423814.1	13 12 22.23	42 38 13.9	0.9	38	2.5564 ± 0.0011	0.4 ± 0.1	550 ± 220	3.0 ± 0.9^c	–
J140955.5+562827^e	14 09 55.50	56 28 26.4	–	17	2.5832 ± 0.0001	2.3 ± 0.2	310 ± 30	–	10.7 ± 0.6^a
J154359.3+535903	15 43 59.43	53 59 03.4	0.7	38	2.3698 ± 0.0006	1.0 ± 0.2	520 ± 140	–	3.8 ± 1.1^a
HS1611+4719	16 12 39.90	47 11 58.3	0.6	37	2.3961 ± 0.0002	1.7 ± 0.3	230 ± 40	–	4.6 ± 0.7^a
MM J163655+4059	–	–	–	39	–	≤ 0.2	–	–	2.2 ± 0.6^d
J164914.9+530316^f	–	–	–	39	–	≤ 0.8	–	–	4.6 ± 0.8^a

Notes:
(a) 1.2 mm flux from Omont et al. (2003)
(b) 850 μm flux from Page et al. (2001)
(c) 850 μm flux from Chapman et al. (2005)
(d) 1.2 mm flux from Greve et al. (2004)
(e) CO parameters from Beelen et al. (2004)
(f) Detected in continuum only
(g) Approximate CO Resolution at the target redshifts, given the beamsizes in Table 1
(h) This quantity was obtained by fitting a Gaussian distribution to the CO spectrum (see text)

3.1.4 RXJ124913.86–055906.2

The integrated CO emission is detected at $\simeq 5\,\sigma$, 1.1 arcsec southeast of the QSO position (Table 2). The CO(3–2) spectrum of RXJ124913.86 has been binned to a frequency resolution of 30 MHz (84 km s^{-1}) and is shown in Fig. 4. We have combined two sets of data with different central frequency tunings (see §2.3) and have arbitrarily set the central frequency to 106.435 GHz, corresponding to CO(3–2) redshifted to $z = 2.2487$. The CO emission line is fitted by a Gaussian profile with a FWHM of 1090±340 km s^{-1}, a velocity-integrated flux density of $S_{\mathrm{CO(3-2)}} = 1.3 \pm 0.4$ Jy km s^{-1}, and a CO redshift of $z_{\rm CO} = 2.2470 \pm 0.0016$, offset by -170 ± 140 km s^{-1} from the near-infrared redshift. This is our broadest CO line detection. No significant continuum emission is detected from the line-free region down to a 1-σ limit of 0.8 mJy.

3.1.5 SMM J131222.35+423814.1

The integrated CO emission of this QSO is marginally detected at $\simeq 2.5\,\sigma$, coincident with the phase centre of the PdBI observations (Table 3). The CO(3–2) spectrum of SMM J131222.35 has been binned to a frequency resolu-

tion of 20 MHz (62 km s^{-1}) and is shown in Fig. 4. The CO emission line is fitted by a Gaussian with a FWHM of 550±220 km s^{-1}, a velocity-integrated flux density of $S_{\mathrm{CO(3-2)}} = 0.4 \pm 0.1$ Jy km s^{-1} (S/N≃3), and a CO redshift of $z_{\rm CO} = 2.5564 \pm 0.0011$ which is consistent with the near-infrared redshift within the 1 σ errors. No significant continuum emission is detected from the line-free region down to a 1-σ limit of 0.1 mJy.

We find a $\simeq 4\,\sigma$ serendipitous emission line in the datacube at 13 12 23.63, 42 38 19.33 (J2000), approximately 15 arcsec northeast[3] of the phase centre, corresponding to a low S/N detected line with a FWHM=450±150 km s^{-1}, $z_{\rm CO} = 2.5408\pm0.0007$, and $S_{\mathrm{CO(3-2)}} = 0.40\pm0.17$ Jy km s^{-1} (S/N≃ 2.5). See Fig. 5. We do not find an optical counterpart for this source down to $K \sim 20$ and $z \sim 24$. If real, this source is offset by 120 kpc and 1300 km s^{-1} from the QSO.

---

[3] Note that the map noise at this distance from the phase centre is only slightly degraded since the primary half power beam width (HPBW) at this frequency is $\simeq 52$ arcsec.

3.1.6   *J140955.5+562827*

We briefly summarise the details for J140955.5 here since its detection is published in (Hainline et al. 2004; Beelen et al. 2004). Beelen et al. (2004) report a CO(3–2) emission detection at the central observed frequency (corresponding to $z_{\rm CO} = 2.5832 \pm 0.0001$) that is well fitted by a Gaussian with a FWHM $= 311 \pm 28\,{\rm km\,s^{-1}}$, yielding $S_{\rm CO(3-2)} = 2.3 \pm 0.2\,{\rm Jy\,km\,s^{-1}}$.

3.1.7   *J154359.3+535903*

We detect the integrated CO emission of this QSO at $\simeq 5\,\sigma$, and coincides with the phase centre of the PdBI observations (Table 3, Fig. 3). The CO(3–2) spectrum of J154349.3 has been binned to a frequency resolution of 20 MHz ($58\,{\rm km\,s^{-1}}$) and is shown in Fig. 4. The CO emission line is well fitted by a Gaussian with a FWHM of $500 \pm 130\,{\rm km\,s^{-1}}$, a velocity-integrated flux density of $S_{\rm CO(3-2)} = 1.0 \pm 0.2\,{\rm Jy\,km\,s^{-1}}$, and a CO redshift of $z_{\rm CO} = 2.3698 \pm 0.0006$ consistent with the near-infrared redshift of the QSO within the $1\,\sigma$ errors. No significant continuum emission is detected from the line-free region down to a 1-σ limit of 0.4 mJy.

3.1.8   *HS1611+4719*

The integrated CO emission in this QSO is detected at $\simeq 6\,\sigma$, 1.3 arcsec north of the phase center of the PdBI observations (see Fig. 3). The CO(3–2) spectrum of HS1611+4719 has been binned to a frequency resolution of 20 MHz ($59\,{\rm km\,s^{-1}}$) and is shown in Fig. 4. The CO emission line is well fitted by a Gaussian with a FWHM of $230 \pm 40\,{\rm km\,s^{-1}}$, a velocity-integrated flux density of $S_{\rm CO(3-2)} = 1.7 \pm 0.3\,{\rm Jy\,km\,s^{-1}}$ (S/N$\simeq$6), and a CO redshift of $z_{\rm CO} = 2.3961 \pm 0.0002$. No significant continuum emission is detected from the line-free region down to a 1-σ limit of 0.5 mJy.

The apparent 1.3 arcsec spatial and $\sim -600\,{\rm km\,s^{-1}}$ velocity offsets between the CO and near-infrared emission might be naturally explained if the CO is associated with a companion galaxy. To test this we search the UIST IFU datacube for a companion galaxy to the north, but are not able to identify any strong line emitting galaxies to a flux limit of $\sim 2 \times 10^{-17}\,{\rm W\,m^{-2}}$ (corresponding to an Hα star-formation rate of $\sim 40\,{\rm M_\odot\,yr^{-1}}$; Kennicutt 1998). We note that the near-infrared spectrum shows an extended blue wing on the [OIII] emission line which is coincident with the redshift of the CO emission (see §2.2). Higher resolution mm spectroscopy and/or deeper near-infrared spectral imaging may be required to determine whether the spatial and velocity offsets arise due to a companion galaxy, an outflow from the QSO, or a merger. This is the only example of a potentially significant offset between the CO and near-infrared position and/or redshifts.

3.1.9   *MM J163655+4059*

Neither CO(3–2) emission nor continuum emission are seen in the map near the QSO position. To calculate a 3-σ upper limit to the velocity-integrated CO(3–2) line flux, we extract a spectrum at the radio position (Table 2) and rebin the spectrum to a frequency resolution of 100 MHz ($310\,{\rm km\,s^{-1}}$) centred on the near-infrared redshift (Table 2), resulting in a channel rms of 0.2 mJy, and we find an upper limit of $0.2\,{\rm Jy\,km\,s^{-1}}$, assuming a line width of $500\,{\rm km\,s^{-1}}$. No significant continuum emission is detected down to a 1-σ limit of 0.2 mJy.

3.1.10   *J164914.9+530316*

No CO(3–2) emission line is seen in this QSO, although continuum emission is detected in the averaged channel map with a flux of 1.6 ± 0.28 mJy (S/N$\simeq$6) at a position of 16 49 14.853, 53 03 16.35 (J2000) (see Fig. 3).

We have determined that the continuum is dominated by synchrotron or free-free emission, with a radio spectral index, α', of 0.1, where $S_\nu \propto \nu^{\alpha'}$, based on 1.4 and 5 GHz fluxes of 820 ± 20 and $910 \pm 80\,\mu$Jy, respectively (Petric et al. 2006) which predicts a 3 mm flux of 1.3 mJy, in agreement with our detection. Based on the 3 mm flux, we estimate that approximately a third of the 1.2 mm flux (1.2 mJy of the $S_{\rm 1.2\,mm} = 4.6 \pm 0.8$ mJy) is due to synchrotron/free-free emission rather than dust emission. We calculate a $3\,\sigma$ upper limit to the continuum-subtracted velocity-integrated CO(3–2) line flux of $0.8\,{\rm Jy\,km\,s^{-1}}$, by rebinning the spectrum to a frequency resolution of 100 MHz ($280\,{\rm km\,s^{-1}}$), resulting in a channel rms of 0.7 mJy, and assuming a line width of $500\,{\rm km\,s^{-1}}$ centred on $z_{\rm NIR} = 2.2704$.

3.2   CO Luminosities and Gas Masses

For each submm-detected QSO, we calculate the line luminosity and estimate the total cold gas mass, $M_{\rm gas}$, from the integrated CO line flux following Solomon & Vanden Bout (2005). We assume a line luminosity ratio of $r_{32} = r_{21} = r = L'_{\rm CO(3-2)}/L'_{\rm CO(1-0)} = 1$ (i.e. a constant brightness temperature). For our QSO sample, we derive a median of $L'_{\rm CO(1-0)} = (3.1 \pm 0.9) \times 10^{10}\,{\rm K\,km\,s^{-1}\,pc^2}$ for the non-detections and a median of $L'_{\rm CO(1-0)} = (4.2 \pm 1.2) \times 10^{10}\,{\rm K\,km\,s^{-1}\,pc^2}$ for only the CO detections (see Table 3). We then convert the CO luminosities into total cold gas masses (including a correction factor for Helium) using $M_{\rm gas} = M({\rm H_2 + He}) = \alpha\,L'_{\rm CO(1-0)}$. We use $\alpha = 0.8\,{\rm M_\odot (K\,km\,s^{-1}\,pc^2)^{-1}}$ as the CO-to-gas conversion factor appropriate for local galaxy populations exhibiting similar levels of star formation activity to submm-bright galaxies or QSOs (e.g. ULIRGs). $r = 1$ and $\alpha = 0.8$ are also used by Greve et al. (2005) for the SMG sample and so our QSOs can be directly compared with SMGs (if these values are appropriate for both populations). The gas masses for our QSOs can be found in Table 4. The median gas mass of the entire sample is $(2.5 \pm 0.7) \times 10^{10}\,{\rm M_\odot}$ when the upper limits are included, and the median gas mass for the CO-detected QSOs is $(3.4 \pm 0.8) \times 10^{10}\,{\rm M_\odot}$. These gas masses are comparable to those observed in higher-redshift ($z \gtrsim 4$) QSOs (e.g. Riechers et al. 2006).

Our observations are of $J \geq 2$ CO transitions, and it is possible that significant amounts of cold, possibly subthermal molecular gas could be present, but only detectable in lower CO transitions. Moreover, if the gas is metal-poor, it is possible that the gas mass could be higher, or we could be missing clumpy dense gas, as these CO observations primarily trace diffuse ISM. Fortunately, these possibilities are unlikely to have a large effect: Riechers et al. (2006) show
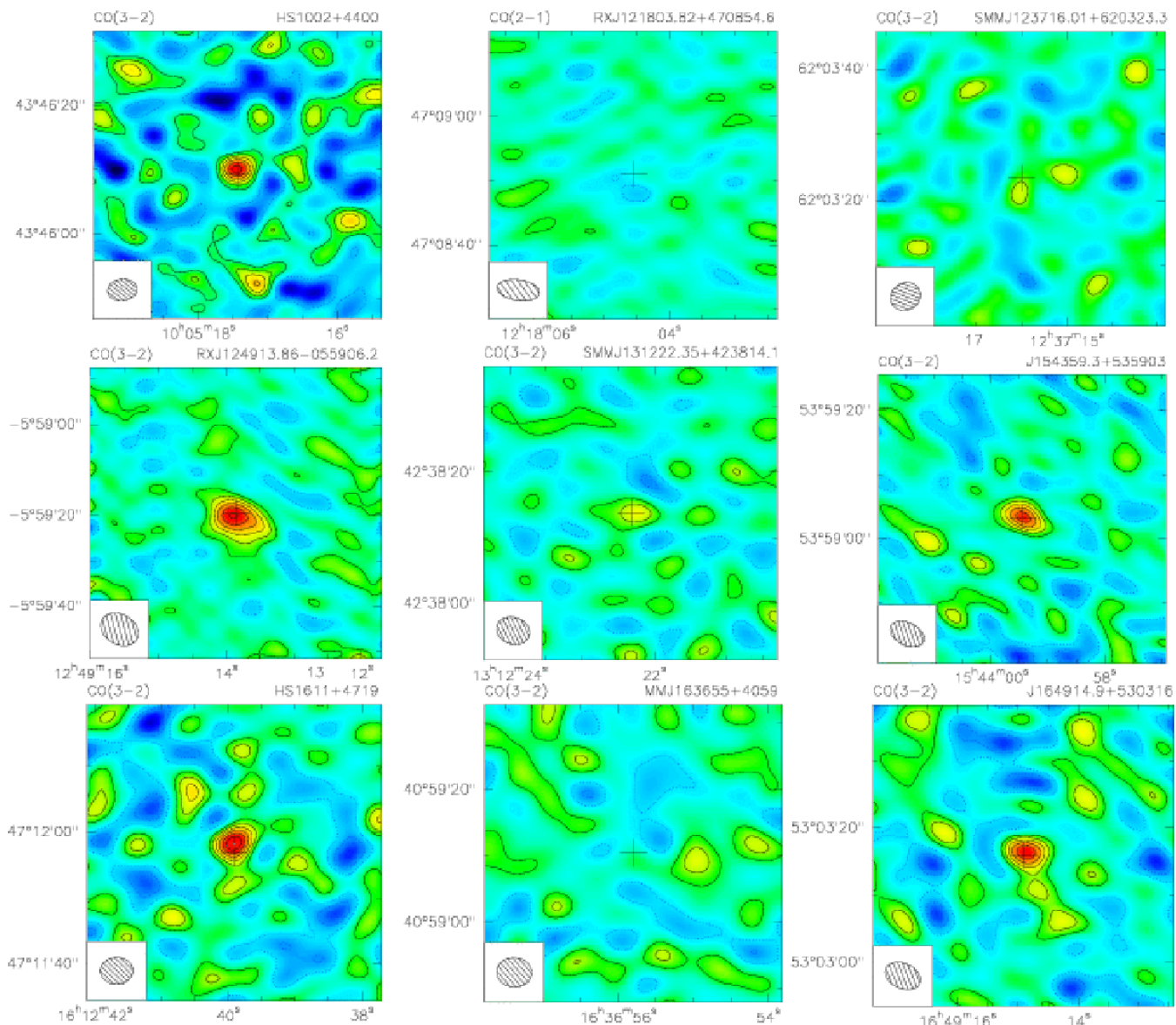
Figure 3. The velocity-integrated mm emission of our nine new submm-detected QSOs. The solid contours are 1, 2, 3... $\times \sigma$ (dashed lines represent equivalent negative contours), where σ refers to the noise in each velocity-integrated map (integrated over the width of the CO line) determined by summing over the weights and includes a contribution from the phase noise visibilities. These are the dirty maps (except for RXJ124913.86 which has been cleaned for presentation here to remove significant sidelobe structure) and the synthesized PdBI beams are shown in the insets as hatched ellipses for reference. Crosses indicate the radio or optical position of each source. *Detections:* The CO-detected sources shown here are HS1002, RXJ124913.86, J131222.35, J154359.3, and HS1611. Note that the CO detection of J131222.35 is marginal. J164914.9 shows a strong continuum detection but no CO detection (see §3.1.10). The positional uncertainties are $\simeq 0.5$, 0.6, 0.9, 0.7, 0.6 and 0.5, respectively, for the CO or continuum detected sources (ranked in RA) based on the S/N of the detections and the beam sizes (see text). *Non-detections:* The three CO and continuum non-detections are shown for comparison and show the 3 mm emission over the central 500 km s^{-1} of the spectra (the average line width of our sample).

that the CO emission in three well-studied $z > 4$ QSOs is well-described by a single centrally-concentrated molecular gas component and is highly excited. But a concern remains that if the CO-to-gas conversion factor for a faint extended component is higher (e.g. Galactic), a higher H$_2$ mass may be hidden in such an extended component. Nevertheless, with suitable caution these observations can still be directly comparable to the SMG sample as they suffer from the same uncertainties and potential biases.

3.3 Line Widths and Dynamical Masses

The median CO line width of our sample is 550 ± 180 km s^{-1} (Table 3). CO line widths can be directly converted into dynamical masses, assuming a size and inclination for the gas reservoirs. In the following we assume a disk model (Solomon & Vanden Bout 2005). Following Tacconi et al. (2006), we derive $v_c \, sin(i)$, where v_c is the circular velocity at the outer CO radius and i is the inclination of the gas disk relative to the sky plane, by dividing the FWHM
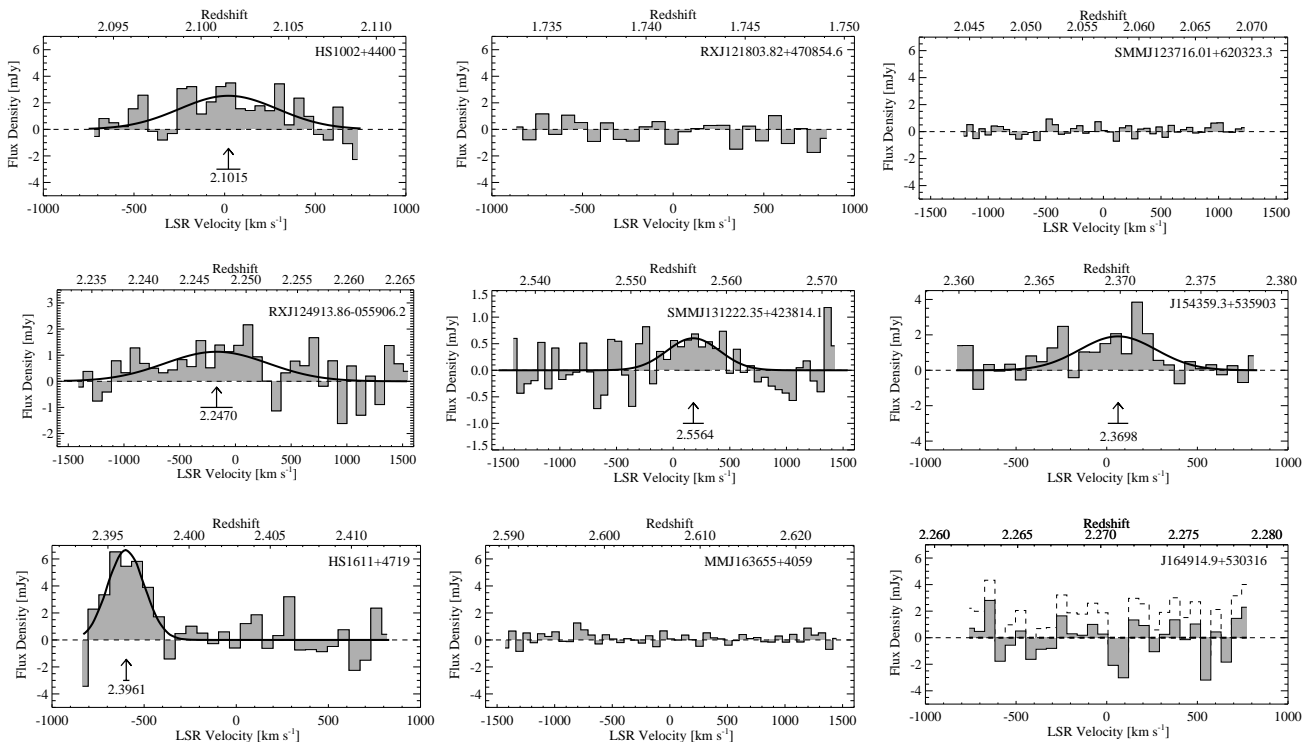
Figure 4. Millimetre spectra of the nine new submm-detected QSOs presented in our sample. The LSR velocity scale is relative to the near-infrared redshift (Table 2) of each QSO, except in the RXJ124913.86, where two central frequency tunings were used, reflecting the uncertainty of the systemic redshift of the source at the time of the CO observations were made, and so we have arbitrarily centered the spectrum on CO(3–2) redshifted to $z = 2.2487$. *Detections:* The CO-detected sources HS1002, J154359.3, J131222.35 and HS1611, have been binned to a frequency resolution of 20 MHz, and RXJ124913.86 has been binned to 30 MHz. The best-fitting CO redshift for each QSO is obtained by fitting each spectrum with a single Gaussian distribution (overplotted) and is indicated by an arrow. See Beelen et al. (2004) for the CO spectrum of J140955.5. *Non-detections:* The CO-undetected spectra have been extracted from the phase tracking centre of the map and have been binned to a resolution of 20 MHz for comparison with the CO detections. The spectrum of J164914.9 has been continuum-subtracted, and the original spectrum is given as the dashed histogram.

of the CO line by 2.4. We calculate the dynamical masses as $M_{\mathrm{dyn}} = R\,v_c^2\,csc^2(i)/G$, where R is the radius of the gas disk which we assume to be 2 kpc, and list these in Table 4. With a typical resolution of ~ 40 kpc for our sample (see Table 3), putting a 2 kpc radius limit is a major assumption (as are assumptions on the system inclination), although we explain why a 2 kpc disk is probably an appropriate assumption for our QSOs in §4.2. We note that our estimates are conservative as the dynamical masses will be higher by a factor of about two if a merger model is adopted (Genzel et al. 2003).

For the CO-detected QSO sample we have a median dynamical mass of $\mathrm{M}(< 2\,\mathrm{kpc}) \simeq (2.5 \pm 1.6) \times 10^{10}\,csc^2(i)$. The main uncertainties in the dynamical mass limits are the assumed disk size and the inclination angle, i. We note that one of our detected QSOs, RXJ124913, has a CO FWHM amongst the largest ever observed for a QSO at any redshift, although our measurement is highly uncertain (the median FWHM for all CO-detected QSOs, including lensed

and $z > 4$ objects, is 300 km s^{-1}; Solomon & Vanden Bout 2005), suggesting that RXJ124913 is viewed at a high inclination angle or that the CO disk size is larger than we have assumed. However, high resolution observations of the CO distribution are needed to better constrain the gas disk sizes, inclination angles, and hence dynamics of our QSOs.

3.4 Far-infrared Luminosities, SFRs and SFEs

We have derived L_{FIR} for the submm-detected QSOs from their restframe far-infrared fluxes and report these in Table 4. We scale a modified greybody model for far-infrared emission to match the 850 or 1200 μm photometry assuming a dust temperature of $T_{\mathrm{d}} = 40$ K and a dust emissivity factor of ν^β, with $\beta = 1.5$ (see e.g. Coppin et al. 2008) and integrate the SED to obtain L_{FIR}. Our assumptions for T_{d} and β agree with the results of Beelen et al. (2006) for three 350 μm-observed QSOs between redshifts of 1.8–2.6 with a
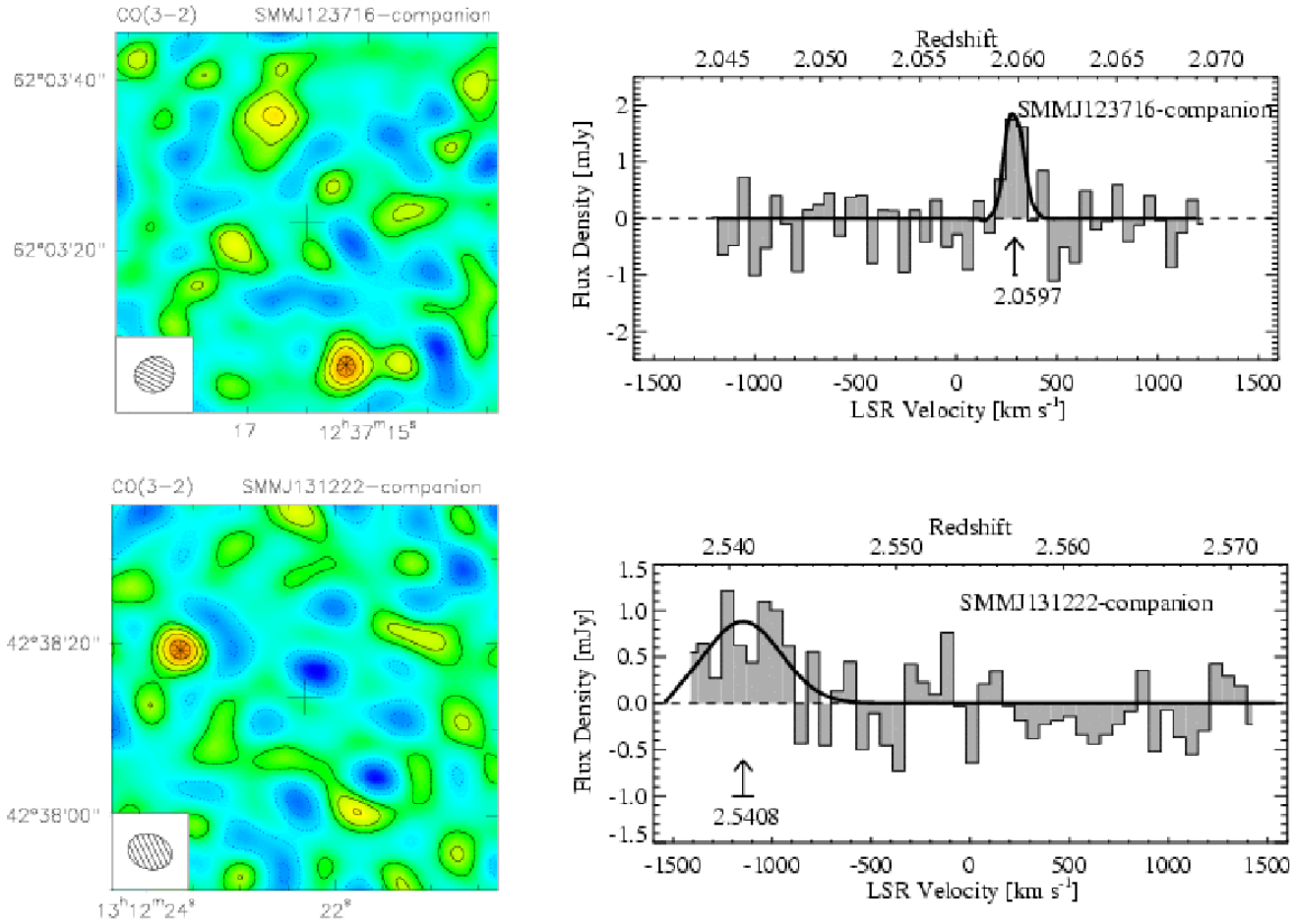
Figure 5. The velocity-integrated mm emission (left) and spectra (right) of serendipitous emission-line candidate 'companion' detections in two of the CO datacubes. See § 3.1.3 and 3.1.5 for details about the individual detections. *Left:* A $\sim 4\,\sigma$ source appears in each map (solid contours are 1, 2, 3... $\times \sigma$), indicated by an asterisk, offset from the PdBI phase centre (indicated by a cross). See the caption of Fig. 3 for details. *Right:* 20-MHz binned spectra are shown for each serendipitous emission-line candidate companion source (see the caption of Fig. 4 for details).

mean fitted $T_{\mathrm{d}} \simeq (35 \pm 7)$ K when β is fixed to 1.6. Note that assuming $T_{\mathrm{d}} = 50$ K effectively increases L_{FIR} by a factor of $\simeq 2.5$ (Wang et al. 2008). We have corrected the observed 1.2 mm flux of J164914.9 by $\simeq$–1.5 mJy, assuming a radio spectral index of 0.1 (see §3.1.10) for synchrotron emission, before computing L_{FIR}.

These L_{FIR} estimates are comparable to those of SMGs (Greve et al. 2005) which is not surprising given the similar submm flux selection criterion. These assume that L_{FIR} is produced predominantly by star-formation as opposed to AGN activity (see discussion in Omont et al. 2003). Recent observations have shown that the L_{FIR} in QSOs is not generally contaminated by AGN, but is due to star formation, even in the most powerful QSOs (e.g. Lutz et al. 2007; Wang et al. 2007), although there are clear exceptions (e.g. Weiss et al. 2007).

This calculation yields a median of $L_{\mathrm{FIR}} = (8.0 \pm 1.9) \times 10^{12}$ L$_{\odot}$ for the submm-detected QSOs. We have converted

L_{FIR} into a star-formation rate (SFR) for our sample following Kennicutt (1998); SFR=1360 $\pm$ 320 $M_\odot$ yr^{-1}. This relation assumes a Salpeter et al. (1955) initial mass function (IMF) and applies to starbursts with ages less than 100 Myr. See Omont et al. (2001) for a discussion of the full range of conversion factors taking into account the uncertainty in the burst age, IMF, and metallicity.

The star formation efficiency (SFE) is a measure of how effective a galaxy is at converting its gas into stars and can be represented by the continuum-to-line ratio, or L_{FIR}/L'_{CO}, as this ratio presumably traces the star formation rate per total amount of gas in a galaxy. We find a median SFE=250$\pm$100 $L_\odot$ (K km s^{-1} pc^2)$^{-1}$ for the full sample of submm-detected QSOs.

3.5 SMBH masses

We determine M_{BH} for our QSOs using the Greene & Ho (2005) virial M_{BH} estimator which calculates the BH mass from the Hα or Hβ emission line widths and fluxes. We can measure these lines from our near-infrared spectra (Fig. 2): the observed emission line properties are given in Table 2 and the BH masses are given in Table 4. We find a median M_{BH} of $(1.8 \pm 1.3) \times 10^9$ $M_\odot$. Note that six out of nine of the submm-detected QSOs have very large BH masses ($M_{BH} \gtrsim 10^9$ $M_\odot$) and are among the largest masses known for local BHs (e.g. Valtonen et al. 2007; Macchetto et al. 1997; Humphrey et al. 2008), and that two objects in the sample are at the upper envelope of known BHs at any redshift, confirming that these BHs are probably hosted by the progenitors of the most massive present-day ellipticals.

Note that we have not corrected the Hα fluxes for extinction, since extinction corrections are rarely applied to broad-line fluxes when estimating virial BH masses, even when rest-frame UV lines are used. Additionally, Alexander et al. (2008) do not find evidence for large amounts of extinction of the broad-line region in their sample of broad-line SMGs (the mean extinction is only $A_V \sim$ 1.2 mags, assuming an intrinsic ratio of Hα/Hβ=3.1 and a Calzetti et al. (2000) reddening law). Applying this mean extinction correction to our sample would increase the BH masses by $\sim$ 15% (0.1 dex). We also investigate whether the Eddington ratios, η, for our submm-detected QSOs are similar to more typical optically selected QSOs in the same redshift range. Following McLure & Dunlop (2004), we calculate the mass accretion rates and Eddington ratios, η, for our submm-detected QSOs and find a range in η consistent with typical QSOs in the same redshift range ($\eta \sim$ 0.1–1; McLure & Dunlop 2004), with a median $\eta \approx 0.7$, which is slightly higher than, but consistent with typical QSOs given the large uncertainties involved.

4 COMPARISON OF THE SUBMM-DETECTED QSOS AND SMGS

We now compare the CO properties of the submm-detected QSOs with SMGs. In order to fairly compare the SMG and QSO samples, we have discarded three strongly lensed galaxies from the CO-observed SMG sample from Greve et al. (2005) that would not have been detected with $\gtrsim$ 5 mJy

at 850 μm. These would lie below our sample flux limit except for the boost from the lensing magnification, and they thus probe an intrinsically fainter population. This leaves a sample of 17 SMGs (of which 11 are CO-detected) from Greve et al. (2005) with a median observed 850 μm flux of 8.2 mJy.

We compare median values of the gas masses, CO linewidths, SFEs, M_{dyn}, and M_{BH}/M_{sph}. The error bars on these median values represent the spread of values, and have been obtained by taking the standard deviation of the median values from 50 trials of randomly drawing out the appropriate number of values out of each population with replacement. We note that the dominant uncertainties in M_{gas}, L_{FIR}, and M_{dyn} are likely the assumed CO-to-gas conversion factor, the assumed β and T_d in the SED fitting, and the assumed CO radius and inclination angle, respectively, and have not been included in each error budget, although the relative M_{gas}, L_{FIR}, and M_{dyn} in our samples will be correct if the same assumptions hold for all our SMGs and submm-detected QSOs.

4.1 The gas masses and star-formation efficiencies of submm-detected QSOs and SMGs

The median gas mass of our CO-detected QSOs is $M_{gas} = (3.4 \pm 0.8) \times 10^{10}$ $M_\odot$ (see Fig. 6). This is similar to the median gas mass of the comparison sample of 11 CO-detected SMGs ($M_{gas} = (3.0 \pm 0.5) \times 10^{10}$ $M_\odot$). Including the upper limits from the CO-undetected objects in each sample yields median gas masses of $(2.5 \pm 0.7) \times 10^{10}$ and $(2.4 \pm 0.5) \times 10^{10}$ $M_\odot$ for submm-detected QSOs and SMGs, respectively. Not surprisingly, we find that the gas mass distributions of both samples are statistically indistinguishable at the present sample sizes, as we show below.

Given the moderate fraction of non-detections in both samples, we employ survival analysis (see e.g. Feigelson & Nelson 1985) to estimate the intrinsic distributions of the gas masses of submm-bright SMGs and QSOs. This includes the detections *and* upper limits, assuming that the data are censored at random (i.e. that the chance of only a gas upper limit being available for an object is independent of the true value of the gas mass). Given the current detection limit and small dynamic range in our sample, there is no strong apparent trend with the selection criteria (i.e. with submm flux) versus whether a particular source is detected or not, and thus the assumption of the data being randomly censored seems reasonable. We employ the widely-used product-limit Avni estimator (Avni et al. 1980; see also Wall & Jenkins 2004) to construct a maximum-likelihood-type reconstruction of the true distribution of gas masses in the QSO and SMG samples (see Fig. 6). We now test whether or not our censored samples of SMG and QSO gas masses are likely to have been drawn from the same distribution using the non-parametric Gehan test, following Feigelson & Nelson (1985). The Gehan statistic yields $L_n = 42 \pm 39$ (equivalent to $\simeq 1\,\sigma$), revealing that the difference between the gas mass distributions for SMGs and QSOs is about 35% likely due to chance. We consider 35% to be a high value, and therefore conclude that the gas masses of our QSO sample are indistinguishable from that of the SMG sample at the same epoch of $z \sim$ 2–3 for the high mass end (where we are the most sensitive).

Table 4. Physical properties of our submm-detected QSO sample derived from the near-infrared and CO observations.

| Source	$L'_{\rm CO}{}^a$ $(\times 10^{10}\,{\rm K\,km\,s^{-1}\,pc^2})$	$L_{\rm FIR}^b$ $(\times 10^{13}\,{\rm L_\odot})$	SFR^c $({\rm M_\odot\,yr^{-1}})$	$M_{\rm gas}^d$ $(\times 10^{10}\,{\rm M_\odot})$	$M_{\rm dyn}\sin^2(i)^e$ $(\times 10^{10}\,{\rm M_\odot})$	$\log M_{\rm BH}$ $({\rm M_\odot})$
HS1002+4400	4.2 ± 0.8	$1.1^{+1.3}_{-0.9}$	1900^{+2200}_{-1600}	3.4 ± 0.7	$3.3^{+1.9}_{-1.5}$	10.14 ± 0.2
RXJ121803.82+470854.6	≤ 2.4	$0.6^{+0.8}_{-0.6}$	1100^{+1400}_{-960}	≤ 1.9	–	–
SMM J123716.01+620323.3	≤ 0.6	$0.5^{+0.7}_{-0.4}$	930^{+1200}_{-620}	≤ 0.5	–	8.1 ± 0.5
RXJ124913.86−055906.2	3.6 ± 1.0	$0.7^{+0.9}_{-0.6}$	1200^{+1500}_{-1000}	2.9 ± 0.8	$9.7^{+7.0}_{-5.1}$	9.76 ± 0.2
SMM J131222.35+423814.1	1.2 ± 0.4	$0.3^{+0.4}_{-0.2}$	520^{+670}_{-360}	1.0 ± 0.3	$2.5^{+2.4}_{-1.6}$	8.2 ± 0.5
VV96 J140955.5+562827	8.2 ± 0.6	$2.7^{+2.9}_{-2.6}$	4600^{+5000}_{-4500}	6.6 ± 0.5	$0.8^{+0.2}_{-0.1}$	9.28 ± 0.2
VV96 J154359.3+535903	3.1 ± 0.7	$1.0^{+1.3}_{-0.7}$	1700^{+2200}_{-1200}	2.5 ± 0.6	$2.0^{+1.2}_{-0.9}$	10.13 ± 0.15
HS1611+4719	5.1 ± 0.8	$1.2^{+1.4}_{-1.0}$	2100^{+2400}_{-1400}	4.1 ± 0.6	$0.4^{+0.2}_{-0.1}$	9.26 ± 0.2
MM J163655+4059	≤ 0.8	$0.6^{+0.7}_{-0.4}$	950^{+1200}_{-690}	≤ 0.6	–	8.4 ± 0.5
VV96 J164914.9+530316	≤ 2.2	$0.8^{+0.9}_{-0.7}{}^f$	1400^{+1600}_{-1100}	≤ 1.8	–	9.16 ± 0.15

Notes:
(a) This quantity was obtained by fitting a Gaussian distribution to the CO spectrum (see text)
(b) Derived assuming $\beta = 1.5$ and $T = 40\,$K (see text)
(c) Derived following Kennicutt (1998) (see text)
(d) Derived assuming $\alpha = 0.8$
(e) Derived assuming a disk radius of 2 kpc
(f) 1.2 mm flux is corrected for synchrotron emission before computing $L_{\rm FIR}$
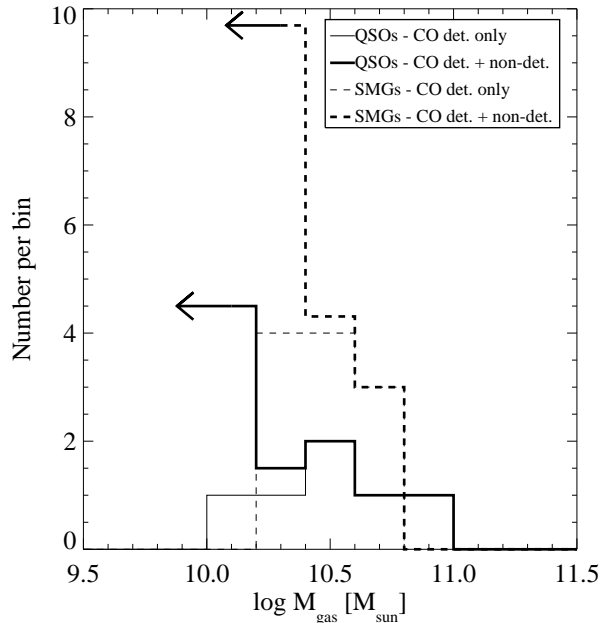
Figure 6. Distribution of the gas masses of the submm-bright QSO and SMG populations. We show an estimate of the cold gas mass distribution of submm-bright QSOs and SMGs, including the CO detections *and* the gas mass upper limits from the non-detections, constructed using the Avni estimator for censored data (see text). Note that the bins containing points $\log M_{\rm gas} < 10.2$ and 10.4 for QSOs and SMGs, respectively, have been made arbitrarily large here since the Avni estimator requires ≥ 1 detection in the lowest bin. The Gehan statistic reveals that the distributions are not significantly different.

Within our QSO sample we find a broad similarity in the star formation efficiency of the CO-detected and undetected QSOs (see § 3.4), assuming conservatively that the CO-undetected subset lies just below the detection threshold. A Kolmogorov-Smirnov (KS) test reveals a 25% chance that the two subsamples are drawn from the same parent population, indicating that we have not detected a statistically significant difference in the SFE between the CO-detected and undetected QSOs in our small sample given the current detection limits. What is the cause then of a given submm-detected QSO in our sample, which all have similar $L_{\rm FIR}$, being either CO-detected versus CO-undetected? A possible explanation could be that the CO-detected submm-detected QSOs are physically larger and contain proportionally more massive CO reservoirs than the CO-undetected QSOs, although time-dependent star formation, differences in the SEDs or filling factors could also be causes for the scatter in the $L_{\rm FIR}$–$L'_{\rm CO}$ correlation (see Fig. 7).

Locally, $L'_{\rm CO}$ increases with $L_{\rm FIR}$ for (U)LIRGs, with the Greve et al. (2005) sample of SMGs extending this trend out to the highest far-infrared luminosities ($\gtrsim 10^{13}\,{\rm L_\odot}$). For comparison, in Fig. 7 we have plotted our QSOs on the $L'_{\rm CO}$–$L_{\rm FIR}$ diagram along with LIRGs, ULIRGs and SMGs. The CO-observed SMGs and QSOs seem to lie along the relation within the considerable uncertainties in their far-infrared luminosities, suggesting that the SMGs and QSOs are undergoing similar star formation modes, despite the QSOs hosting luminous AGN activity.

To quantify this we compare the SFE of the QSOs to the SMGs, where $L_{\rm FIR}$ for the SMGs has been calculated using the method outlined in §3.4 and their $L'_{\rm CO}$ are taken from Greve et al. (2005). As Fig. 7 shows, the SMGs appear to have similar SFE with respect to QSOs on average, although this probably reflects the similar submm flux selection criteria. Given that the median $L_{\rm FIR}$ and $M_{\rm gas}$ of the QSO and SMG samples are similar, $(8.0\pm1.9)\times10^{12}\,{\rm L_\odot}$ and $(7.9 \pm 0.8) \times 10^{12}\,{\rm L_\odot}$ and $(2.5 \pm 0.7) \times 10^{10}\,{\rm M_\odot}$ and $(2.4 \pm 0.5) \times 10^{10}\,{\rm M_\odot}$ (including all CO-detected and -undetected QSOs and SMGs), respectively, the SFEs are also similar: medians of 250 ± 100 and $260 \pm 50\,{\rm L_\odot\,(K\,km\,s^{-1}\,pc^2)^{-1}}$, for QSOs and SMGs respectively. We perform a Gehan test on these censored data sets and find $L_{\rm n} = 56\pm35$ ($\simeq 1.6\,\sigma$), revealing that the difference between the distribution of SFE in SMGs and QSOs is about 15% likely due to chance, indicating that we have not detected a significant difference in the SFE between our small samples of SMGs and QSOs.
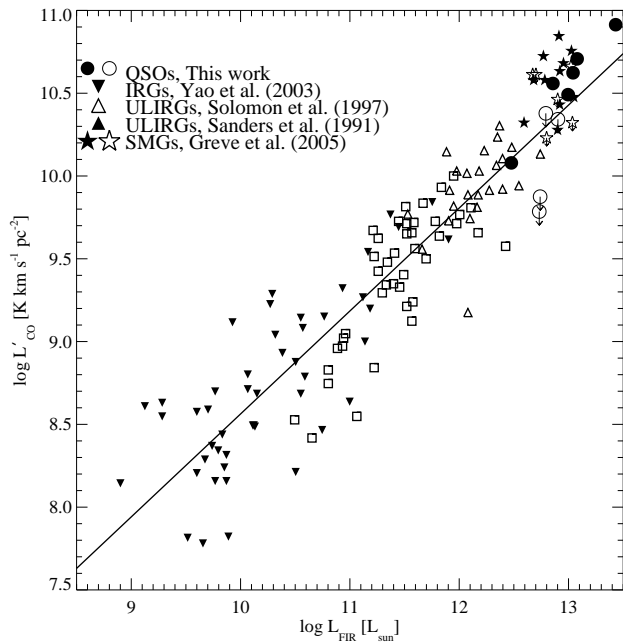
Figure 7. Comparison of the CO and far-infrared luminosities for QSOs, LIRGs, ULIRGs, and SMGs. The line is the best-fitting relation with a form of $\log L'_{\rm CO} = \alpha \log L_{\rm FIR} + \beta$ to the LIRGs, ULIRGs and SMGs from Greve et al. (2005). The CO-observed SMGs and QSOs appear to occupy the same part of the diagram (filled circles/stars represent CO-detections and open circles/stars are CO-nondetections), and lie just above the relation though the offset is not significant given the large errors in $L_{\rm FIR}$. This is a particularly useful diagnostic, since it does not depend on the CO-to-gas conversion factor.

4.2 The CO line profiles and dynamical masses of submm-detected QSOs and SMGs

A comparison between the observed CO line profiles of SMGs and QSOs requires care as we know that there is an inherent difference in the types of lines seen in SMGs versus QSOs: five of the 11 SMGs detected in CO in our comparison sample show hints of double-peaked profiles (Greve et al. 2005; Tacconi et al. 2006), while none of our QSO CO emission lines appear double-peaked (which is perhaps not surprising given our small sample size and low SNR data). These double-peaked profiles could indicate merger activity (as likely for SMGs from high-resolution observations), or a rotating gas disk/ring (e.g. Genzel et al. 2003). In both cases, measuring the separation between the peaks is a more appropriate measure of the dynamics of the merger or rotating disk system than the FWHM of the individual peaks.

In cases where double-peaked profiles are present we need to fit two Gaussian profiles simultaneously in order to derive the velocity offsets of the peaks. We have therefore refit all of the SMGs and QSOs with single and double Gaussian profiles using the χ^2 statistic as a measure of the goodness-of-fit. We find that 4/11 of the CO-detected SMGs are better fit at the $> 3.5\,\sigma$ level with a double Gaussian profile over a single Gaussian profile (Greve et al. 2005). None of the submm-detected QSOs are significantly better fit by double Gaussian profiles, although we note that the random chance of drawing six single peaked profiles (with replace-

ment) out of a sample containing seven single-peaked and four double-peaked profiles (i.e. the SMG sample above) is 7 percent. The fact that the QSO profiles appear to be single-peaked could indicate that our data are too low SNR to detect double-peaked profiles (especially for a merger, where both the width and peak strength of the lines can be different), or that we are viewing the QSOs almost face-on[4] if the CO is contained in a disk, or that they are at a late stage of a merger, or that they are not in the course of a merger.

For our six submm-detected QSOs we compare the CO FWHMs and dynamical masses with the CO-detected subsample of 11 SMGs taken from the literature (Greve et al. 2005; Tacconi et al. 2006). The median FWHM of the six CO-detected QSOs and seven single-Gaussian profile fit SMGs are (550 ± 180) and $(600 \pm 130)\,{\rm km\,s^{-1}}$, respectively. When we include the double Gaussian profile fits in the median estimate, taking the separation between the peaks as a proxy for the dynamics of the system, the median for the SMGs slightly decreases to $(530 \pm 110)\,{\rm km\,s^{-1}}$. We have plotted the histogram of the submm-detected QSO and SMG line widths for comparison in Fig. 8 (c.f. fig. 2 in Carilli & Wang 2006).

The CO FWHM of QSOs and SMGs appear to be similar. To quantify this we use a standard two-sided KS test which reveals a 95% probability that the two distributions are drawn from the same parent population (this drops to 77% if only the single-line Gaussian profile SMGs are used). This is in stark contrast with Carilli & Wang (2006), who find only a 0.9% probability for an inhomogeneous sample of 12 SMGs and 15 QSOs from a literature compilation (Solomon & Vanden Bout 2005). However, we note that they have used the SMG single-Gaussian profile fit line widths even in cases where clearly double-peaked CO profiles are apparent, leading to artificially broad FWHM in these cases. Their analysis is also based on a mixed sample over a wide redshift range and includes strongly lensed sources. Also, the QSOs studied here have larger linewidths than have been reported for other QSOs and they are also those with the lowest SNRs and thus the most difficult to fit. Therefore the differences in our results for $z \sim 2$ QSOs and those in Carilli & Wang (2006) for higher redshift QSOs can probably mainly be attributed to the small sample sizes involved and the somewhat different approaches (rather than a real statistically significant effect) when all possible sources of error are taken into account.

Since the CO line widths of SMGs and QSOs are simi-

---

[4] An intrinsically double peaked profile could appear single-peaked if the velocity offset between the peaks is small enough (e.g. at high SNR a close merger could show an asymmetric line profile, hinting at two components). We attempt to put a limit on the inclination angles in our data by investigating a simple test case. We take two Gaussian distributions with $\sigma = 150$–$220\,{\rm km\,s^{-1}}$ (similar to those found for double-peaked SMGs) and equal line fluxes and shift them to a velocity separation such that the FWHM of a single-Gaussian profile fit is $\simeq 550\,{\rm km\,s^{-1}}$ (our QSO sample median FWHM), yielding typical velocity separations of 300–150 km s^{-1}. This translates into a conservative limit on the inclination of the system of $i \lesssim 40°$ by using the relation $v_{\rm obs} = v_{\rm circ}\,sin(i)$ and taking $v_{\rm obs} \simeq 250\,{\rm km\,s^{-1}}$ and $v_{\rm circ} = 400\,{\rm km\,s^{-1}}$ (the latter value is what is observed typically for SMGs by fitting double Gaussian profiles).
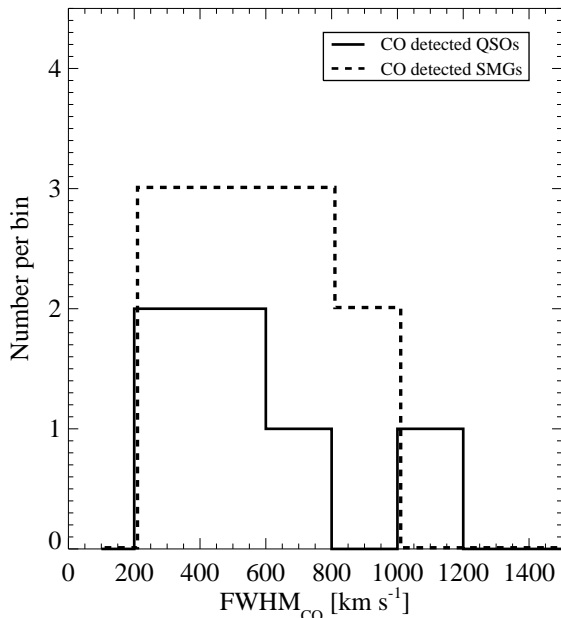
Figure 8. Comparison of the distributions of CO FWHM for 11 SMGs and 6 QSO with detected CO emission. The distributions have medians of $(530 \pm 110)\,\mathrm{km\,s^{-1}}$ (for a mix of single and double Gaussian profile fits), and $(550 \pm 180)\,\mathrm{km\,s^{-1}}$ for SMGs and QSOs, respectively. A KS test reveals a 95% probability that the SMG and QSO CO FWHM distributions are drawn from the same parent population (see text). The histograms have been offset slightly for clarity.

lar, it may follow that the dynamical masses of SMGs and QSOs are also similar. The uncertainties in this are if the gas is distributed similarly in both populations (i.e. either a disk or merger scenario), if their sizes (R) are the same, and if their average inclination angles (i) are similar. $R \simeq 2\,\mathrm{kpc}$ is believed to be appropriate for the gas distribution in SMGs (e.g. Greve et al. 2005; Tacconi et al. 2006, 2008). One of our QSOs, J140955.5, has been observed at PdBI by Beelen et al. (2004) in CO(7–6) with a $1.0'' \times 0.5''$ resolution and was unresolved, giving an upper limit to the gas reservoir of $5\,\mathrm{kpc}$ (though this could be too high a J transition to trace the bulk of the gas reservoir). No sizes have been measured for our sample of QSOs, although the CO emission seems to be confined to a compact region in other samples of high-z QSO (Riechers et al. 2006) as inferred by comparing a range of CO line ratios (see also Walter et al. 2004 who observe gas distributed over a 2.5 kpc radius and Riechers et al. 2008). This agrees with the recent results from Maiolino et al. (2007) who find that CO emission in a $z \simeq 5$ QSO is unresolved with a beam size of $\sim 1\,\mathrm{arcsec}$, implying that the molecular gas is contained within a compact region with a radius of $< 3\,\mathrm{kpc}$. The QSO from Maiolino et al. (2007) was observed in a high J transition, CO(5–4), and one might worry that such high transitions might not trace the bulk of the reservoir. CO(1–0) and (2–1) observations of other $z \gtrsim 4$ QSOs (e.g. Riechers et al. 2006) have confirmed that the high J transitions do trace the bulk of the reservoir, and thus provide good size constraints (this is in contrast to what is observed in most nearby galax-

ies). Spatially resolved observations exist for local QSOs, albeit the data are sparse: Downes & Solomon (1998) measure a $R \gtrsim 1\,\mathrm{kpc}$ disk in Mrk 231; Staguhn et al. (2004) find a $R \gtrsim 1\,\mathrm{kpc}$ ring-like molecular gas distribution; and Krips et al. (2007) estimate $R \simeq 3 \pm 1\,\mathrm{kpc}$ for the CO emission in a low luminosity QSO. Therefore, assuming 2–3 kpc radius regions will probably still be reasonable once these galaxies are resolved.

While the average orientation of the SMGs is likely to be close to the value expected for random orientations, $i \simeq 30°$, since they are not prone to orientation selection effects (see Carilli & Wang 2006), the submm-detected QSOs could be orientated preferentially with respect to the sky plane due to their selection as optically luminous QSOs in the first place. We find evidence for this from a comparison of the [OIII] line width (see Table 2), a proxy for the measure of the stellar velocity dispersion (supporting the idea that the narrow-line region gas is in orbital motion in the gravitational potential well of the bulge; Nelson & Whittle 1996; Nelson 2000; Bonning et al. 2005), with the CO line width. We find that the [OIII] FWHM are a median factor of 1.9 ± 0.5 broader than the CO line profiles (with a large scatter; ratios range from 0.6–4.3), suggesting indeed that inclination effects could be important in the CO line widths of QSOs (see also Shields et al. 2006). The lack of the double-peaked CO profiles in the submm-detected QSOs could be interpreted as a later phase of a merger in the typical proposed evolutionary sequence, with SMGs representing an earlier phase of the merger. We also know that at least two of our QSOs must have $i \lesssim 20$ (alternatively the assumed standard CO-to-H_2 conversion factor could be too high or else the assumed 2 kpc radius is too small) or else the cold gas mass estimates exceed the dynamical masses (even given the large error bars; see Table 4). Conversely, some of our broadest CO line detections suggest that their inclination angles might be larger than $20°$. Other constraints come from the obscured:unobscured AGN ratio ($\simeq 5$–10) for a sample of SMGs, where Alexander et al. (2008) suggest that QSOs could be seen close to the line of sight ($i = 18$–$25°$). We thus adopt the best available estimates of the average inclination angles for SMGs and QSOs of $30°$ and $20°$, respectively, in calculating the dynamical masses below. High-resolution CO observations could help to place tighter constraints on the inclination angles of our systems.

Assuming a 2 kpc radius and an average inclination angle of $20°$ for the submm-detected QSOs and $30°$ for the SMGs, we find median dynamical masses, $M_{\mathrm{dyn}} \propto \mathrm{FWHM_{CO}}^2\, R\, csc^2(i)$, of $M(< 2\,\mathrm{kpc}) \simeq (2.1 \pm 1.4) \times 10^{11}$ and $(0.9 \pm 0.4) \times 10^{11}\,\mathrm{M_\odot}$, respectively. This results in gas-to-dynamical mass fractions of $\sim 15\%$ and 30% for QSO and SMG populations, respectively. The gas mass accounts for a significant fraction of the dynamical mass of both classes, indicating that the host galaxies are at an early evolutionary stage.

4.3 The BH-spheroid ratios of submm-detected QSOs

We place a constraint on the spheroid mass by taking the dynamical mass estimate from §4.2, assuming $i = 20°$ and a spheroid radius of 2 kpc or less (as we assumed for the CO emission), yielding a median spheroid mass of $M_{\mathrm{sph}} =$
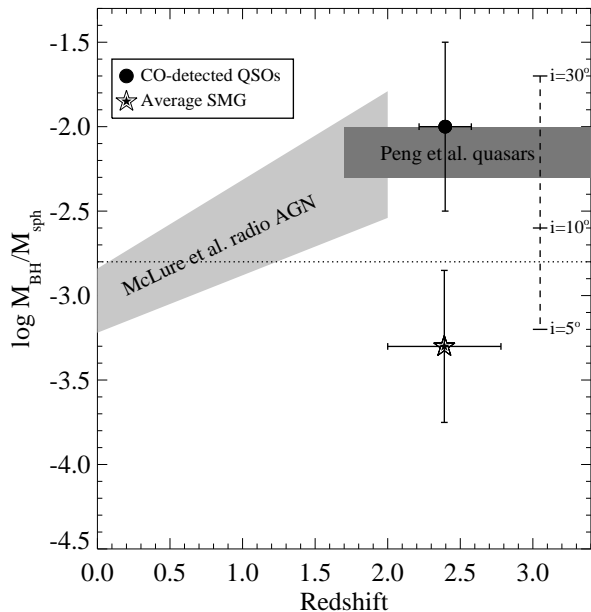
Figure 9. The variation in $M_{\mathrm{BH}}/M_{\mathrm{sph}}$ with redshift, z, for different populations of galaxies and AGN. We show the ratio measured for BHs in local spheroids (dotted line; Häring & Rix 2004) and those inferred for high-redshift radio-loud AGN (McLure et al. 2006), QSOs (Peng et al. 2006), and SMGs (Alexander et al. 2008). We compare these to the ratio determined for our CO- and submm-detected QSOs. We find good agreement between our estimate and that of Peng et al. (2006) for similar, optically luminous QSOs at $z \sim 2$, supporting the assumptions used in our analysis, although we show how our estimate changes for different assumed inclination angles (dashed lines). Similarly, the typical QSO detected in our survey has a significantly higher $M_{\mathrm{BH}}/M_{\mathrm{sph}}$ ratio than inferred for $z \sim 2$ SMGs.

$(2.1 \pm 1.4) \times 10^{11}\,\mathrm{M}_{\odot}$. In principle one should subtract the gas and BH masses, although we note that doing so makes a negligible difference in general, given the large error bars on M_{dyn}, and we also have an additional complication that two of our CO-detected QSOs have $M_{\mathrm{gas}} > M_{\mathrm{dyn}}$. Other uncertainties to our M_{sph} estimates include the possibility that the cold gas in submm-detected QSOs is more widely distributed (e.g. due to entrainment in outflows) than we have assumed here ($\gtrsim 2\,\mathrm{kpc}$), which would mean that all of our dynamical (and hence spheroidal) masses have been underestimated. Similarly, if the spheroid is significantly more extended than the CO emission then the spheroid masses will be larger. For example, assuming a characteristic radius of $\sim 10\,\mathrm{kpc}$ for the spheroid would result in an increase in the mass of a factor of ~ 5 times.

Based on these assumptions we estimate $M_{\mathrm{BH}}/M_{\mathrm{sph}} \sim (9^{+21}_{-6}) \times 10^{-3}$ for our QSO sample. This is approximately an order of magnitude larger than the local ratio of $(1.4 \pm 0.4) \times 10^{-3}$ for the BHs in local spheroids (Fig. 9; Marconi & Hunt 2003; Häring & Rix 2004). Thus our CO survey of $z \sim 2$ QSOs appears to support the claim that $M_{\mathrm{BH}}/M_{\mathrm{sph}}$ for $z > 1$ AGN is higher than observed locally (e.g. Peng et al. 2006; McLure et al. 2006). Our $M_{\mathrm{BH}}/M_{\mathrm{sph}}$ ratio could be made to match the local relation by either decreasing the inclination angles to $\sim 6^{\circ}$ or by adopting a spheroid extent

ten times larger than we have assumed. Our results and those of Peng et al. (2006) suggest that BH growth may occur more rapidly than spheroid formation in QSOs at $z \sim 2$ (although both studies could be prone to strong selection effects; see Alexander et al. 2008). Similar CO-based studies of rarer individual QSOs at higher redshifts also support this conclusion (e.g. Walter et al. 2004; Maiolino et al. 2007).

This result contrasts strongly with the $M_{\mathrm{BH}}/M_{\mathrm{sph}}$ claimed for SMGs, which lie just below the local ratio (Fig. 9; Alexander et al. 2008). However, as mentioned in §3.5, six out of nine of our submm-detected QSOs have very massive BHs ($M_{\mathrm{BH}} \gtrsim 10^9\,\mathrm{M}_{\odot}$) which are far more massive than those inferred for typical SMGs (Alexander et al. 2008; $M_{\mathrm{BH}} \approx 10^8\,\mathrm{M}_{\odot}$) and would place them among the largest known masses for local BHs. They are therefore likely to be considerably rarer than typical SMGs. To make a fairer comparison between SMGs and submm-detected QSOs we need to focus on those CO-detected submm-detected QSOs with M_{BH} more similar to that found for SMGs. We have three submm-detected QSOs in our sample with BHs more similar to those of SMGs, unfortunately two of these are undetected in CO, so we cannot determine their dynamical masses. Nevertheless, the one example with a marginal CO detection, SMM J131222.35, has an implied spheroid mass of $M_{\mathrm{sph}} = 2.1 \times 10^{11}\,\mathrm{M}_{\odot}$ (assuming $i = 20^{\circ}$) and hence $M_{\mathrm{BH}}/M_{\mathrm{sph}} \simeq 9 \times 10^{-4}$. This is an order of magnitude below the ratio for the more optically luminous QSOs and places SMM J131222.35 approximately on the local relation (Fig. 9). While based on a single source marginally detected in CO, this result hints that submm-detected QSOs with $M_{\mathrm{BH}} \simeq 10^8\,\mathrm{M}_{\odot}$ might be the SMG–QSO 'transition' objects we are interested in. We discuss this possibility further in §5.

5   DISCUSSION OF THE EVOLUTIONARY STATUS OF SUBMM-DETECTED QSOS

In this section we discuss the various observations which constrain the evolutionary relationship between SMGs and submm-detected QSOs. For the purposes of this discussion, we adapt the proposed evolutionary pathway of Sanders et al. (1988) and so test the scenario where the SMG population evolves through a submm-detected QSO phase, into a submm-undetected QSO and finally a passive elliptical. Now we ask – are the observed properties of the SMGs and submm-detected QSOs consistent with their observed gas depletion, amount of BH growth, and space densities required to link them in this evolutionary sequence?

To provide a characteristic timescale for our discussion we first determine the lifetime of the submm-detected QSO phase. We assume that the far-infrared luminosities of the submm-detected QSOs arise from dust-obscured star formation and that the molecular gas reservoirs we detect via their CO emission are the fuel for this star formation. In this way we determine that the QSOs have enough cold gas to sustain their current episode of star formation (assuming a star formation efficiency of 100%) for $\tau_{\mathrm{depletion}} \sim M_{\mathrm{gas}}/\mathrm{SFR} \sim 2.5 \times 10^{10}\,\mathrm{M}_{\odot}/1360\,\mathrm{M}_{\odot}\,\mathrm{yr}^{-1} \sim 20\,\mathrm{Myr}$. $\tau_{\mathrm{depletion}}$ is on the order of a couple of dynamical times within our assumed CO radius of $2\,\mathrm{kpc}$ ($\tau_{\mathrm{dyn}} = R/v_{\mathrm{c}} < 9\,\mathrm{Myr}$), which could be defined as a 'maximal starburst' (e.g. Tacconi et al. 2006)

as is commonly found with other populations of starburst galaxies such as ULIRGs at low-redshift and SMGs and other QSOs at high-z. Since we are most likely catching the QSOs halfway through the current star formation episode, we infer a submm-detected QSO phase lifetime of $2 \times \tau_{\mathrm{depletion}} = 40\,\mathrm{Myr}$. The reader should of course note that $\tau_{\mathrm{depletion}}$ and our estimated lifetime are both lower limits if L_{FIR} includes a significant contribution from AGN activity, or if the starburst is discontinuous, or if the IMF is more top heavy than Salpeter's IMF, or if the gas reservoirs contain significant masses of sub-thermal gas (Greve et al. 2006), or if the CO reservoir is widely distributed on scales $\gg 30\,\mathrm{kpc}$ (not that there is any evidence that such galaxies exist).

Next we note that in our submm-detected QSO sample CO is typically detected in only the optically luminous QSOs (see Fig. 1), i.e. those QSOs with the most massive BHs ($M_{\mathrm{BH}} > 10^9\,\mathrm{M}_{\odot}$; see Fig. 10). As we discussed in §4.3 these BHs are much more massive than found in typical SMGs – is it feasible for the BHs to grow sufficiently between these two phases? In Fig. 10 we plot M_{gas} as a function of M_{BH} for our sample of submm-detected QSOs and for an 'average' SMG (M_{BH} from Alexander et al. 2008 and M_{gas} from Greve et al. 2005). We indicate gas consumption and BH growth evolutionary tracks for the average SMG on timescales of 10 and 20 Myr, assuming a SFR of $1000\,\mathrm{M}_{\odot}\,\mathrm{yr}^{-1}$ and Eddington-limited BH growth. Fig. 10 demonstrates that an SMG could evolve into a submm-detected QSO with $M_{\mathrm{BH}} \simeq 10^8\,\mathrm{M}_{\odot}$ and $M_{\mathrm{gas}} \simeq 0.6 \times 10^{10}\,\mathrm{M}_{\odot}$ (the median M_{gas} of the CO-undetected QSOs) in a reasonable timescale, whereas an average SMG would need substantially (~ 10 times) more gas and more time ($\gtrsim$ SMG lifetime) to evolve into the optically luminous submm-detected QSOs in our sample with $M_{\mathrm{BH}} \simeq 4 \times 10^9\,\mathrm{M}_{\odot}$ and $M_{\mathrm{gas}} \simeq 3.0 \times 10^{10}\,\mathrm{M}_{\odot}$.

The gas consumption and BH growth timescales suggest that the optically luminous submm-detected QSOs in our sample cannot be the direct descendents of typical SMGs. Indeed the CO-detected optically luminous QSOs in our sample are extremely luminous AGN ($M_{\mathrm{B}} \approx -28$, Omont et al. 2003) with $M_{\mathrm{BH}} > 10^9\,\mathrm{M}_{\odot}$ and will most likely evolve into the most massive elliptical galaxies found in local rich clusters. These QSOs are so rare ($\simeq 2\,\mathrm{deg}^{-2}$ over all redshifts; Fan et al. 2001) that they are unlikely to be associated with *any* known SMGs, since $S_{850\,\mu\mathrm{m}} > 4.5\,\mathrm{mJy}$ SMGs at $z = 1$–3 have much higher surface densities ($\simeq 600\,\mathrm{deg}^{-2}$; Coppin et al. 2006) or space densities ($\simeq 10^{-5}\,\mathrm{Mpc}^{-3}$; Chapman et al. 2005). Even correcting for the relative timescales of the two phases still leaves an order of magnitude difference in the space densities. Based on the relative number or space densities, these optically luminous submm-detected QSOs are unlikely to be involved in the SMG/QSO evolutionary sequence we are interested in testing.

In contrast, the less luminous submm-detected QSOs appear to be consistent with the Sanders et al. (1988) proposed evolutionary sequence, linking them to typical SMGs (see Fig. 10). Thus we concentrate on the three submm-detected QSOs (including one marginal CO detection and two upper limits: SMM J131222.35, SMM J123716.01 and MM J163655) with BHs more similar to that of SMGs of $M_{\mathrm{BH}} \simeq 10^8\,\mathrm{M}_{\odot}$. The median gas mass and SFR of this subsample are $0.6 \times 10^{10}\,\mathrm{M}_{\odot}$ and $850\,\mathrm{M}_{\odot}\,\mathrm{yr}^{-1}$, respectively.

Hence, these systems can sustain their current star formation episode for $\tau_{\mathrm{depletion}} \lesssim 7\,\mathrm{Myr}$ or a total lifetime of the submm-detected QSO phase of $\lesssim 15\,\mathrm{Myrs}$. This estimate of the lifetime of submm-detected QSOs can then be used to relate them to SMGs as follows. The incidence of blank-field submm sources identified with QSOs is $\sim 4\%$ (Chapman et al. 2005). In our test scenario this is the fraction of an SMG lifetime in which it appears as an submm-detected QSO. Conversely, about 15–25% of optically luminous QSOs are detected in the submm (Omont et al. 2003). Assuming that all bright SMGs go through a QSO phase, and that all QSOs are formed via SMGs and there is no strong mass or luminosity dependence of their lifetimes, then these relative fractions imply that the total QSO lifetime (i.e. submm-detected plus submm-undetected) is about $20\%/4\% = 5$ times shorter than the average lifetime of an SMG. Taking our estimated lifetime of less luminous submm-detected QSOs, $\lesssim 15\,\mathrm{Myrs}$, these detection fractions imply total lifetimes for QSOs of $\lesssim 70\,\mathrm{Myrs}$ and for SMGs $\lesssim 350\,\mathrm{Myrs}$. These estimates are consistent with independent estimates of the lifetimes for QSOs of ~ 20–$40\,\mathrm{Myr}$ (Martini & Weinberg 2001; Goncalves et al. 2008) and ~ 100–$300\,\mathrm{Myr}$ for SMGs from modelling (Swinbank et al. 2006).

There are two other observational links between these QSOs with $M_{\mathrm{B}} \approx -25$ ($M_{\mathrm{BH}} \sim 5 \times 10^8\,\mathrm{M}_{\odot}$) and SMGs. Firstly, the QSOs have space densities at $z \sim 2$ some 5–10 times lower than SMGs (Boyle et al. 2000; Chapman et al. 2003). This ratio of volume densities is roughly consistent with the ratio of the relative SMG and QSO lifetime, ~ 100–$300\,\mathrm{Myrs}$ and ~ 20–$40\,\mathrm{Myrs}$, of ~ 5 times. Moreover, in §4.3 we found a hint that this subset of our submm-detected QSOs lies on the present-day $M_{\mathrm{BH}}/M_{\mathrm{sph}}$ relation and similar to SMGs, which is consistent with them being 'transition objects' between SMGs and QSOs in the proposed evolutionary sequence in which they would eventually evolve into passively evolving spheroids.

Although this conclusion is based on a small sample of QSOs, if the dynamical and gas properties of these three QSOs are representative of this subset of submm-detected QSOs, then our results are consistent with $\sim L^{\star}$, $M_{\mathrm{BH}} \simeq 10^8\,\mathrm{M}_{\odot}$ submm-detected QSOs being 'transition objects' in the proposed evolutionary sequence, representing a very brief prodigious star formation phase where the BH is undergoing rapid growth synchronously with the stellar mass. Submm-detected QSOs do not possess sufficiently large gas reservoirs (containing less gas than SMGs on average) to sustain the implied SFRs for very long, providing a possible explanation for why some of our submm-detected QSOs are undetected in CO (a single weak CO detection and two non-detections of $M_{\mathrm{BH}} \simeq 10^8\,\mathrm{M}_{\odot}$ submm-detected QSOs).

Where do the optically luminous submm-detected QSOs fit into this evolutionary scheme? The average SMG would need $\approx 1\,\mathrm{Gyr}$ (more than its lifetime) in order to grow their BHs by the required factor of $\gtrsim 60$ to host a $M_{\mathrm{BH}} \simeq 4 \times 10^9\,\mathrm{M}_{\odot}$ BH seen in the optically luminous subset of submm-detected QSOs. In addition, these SMGs would need to begin with gas reservoirs containing $M_{\mathrm{gas}} \gtrsim 4 \times 10^{11}\,\mathrm{M}_{\odot}$ in order to leave luminous QSOs with detectable reservoirs of residual gas. Alternatively, these rare optically-luminous QSOs could be periodically 'repeating'

SMGs, with SMG progenitors with $M_{\rm gas} \gtrsim 10^{11}\,M_\odot$ and a surface density of $\simeq 10\,{\rm deg}^{-2}$, which are consuming their gas and growing their BHs synchronously, but which accumulate additional BH mass and gas through merging with other SMGs in dense environments (i.e. damp 'dry merging'; e.g. Bell et al. 2004). However, we currently have not observed any SMGs with such large gas masses, and given their rarity, we will require large scale submm blank-field surveys such as those planned with SCUBA-2 to find these potential progenitor SMGs.

Hence our current results split the submm-detected QSOs in our survey into two categories (although a bigger sample would probably give a continuous trend):

(1) Our observations of the optically luminous submm-detected QSOs indicate they have $M_{\rm BH} > 10^9\,M_\odot$. It is very difficult to grow the BHs in typical SMGs to such large masses in the typical lifetimes of SMGs or submm-detected QSOs. We therefore suggest that these QSOs cannot be related to the evolutionary cycle of typical SMGs. Instead, these intrinsically rare QSOs most likely evolve from an equally rare subset of the SMG population – whose surface density is low enough that it has yet to be detected in current small-area submm surveys. Simply based upon the masses of their BHs, it is clear that these systems can only evolve into the most massive elliptical galaxies found in local rich clusters.

(2) We have found a subset of our submm-detected QSOs with lower optical luminosities which have gas and BH masses and space densities which are consistent with them being potential 'transition objects' in the proposed evolutionary scenario where SMGs evolve into QSOs. This subset of submm-detected QSOs have $M_{\rm BH} \simeq 10^8\,M_\odot$ and gas consumption timescales consistent with a phase of prodigious star formation where the BH has grown substantially during the preceding $\sim 200\,{\rm Myr}$ SMG phase. The fast build up of the stellar population is consistent with an evolutionary path ending in a population of present-day massive spheroids, where homogeneous old stellar populations are seen (Swinbank et al. 2006).

6   CONCLUSIONS AND FUTURE WORK

We have carried out a millimetre interferometry survey of nine submm-detected QSOs at $z = 1.7$–2.6 in order to test the link between SMGs and QSOs at the era where these two important populations were most numerous. We include in our analysis comparable observations of a similarly selected QSO from the literature to provide a final sample of ten submm-detected QSOs. To support this survey we obtained near-infrared spectroscopy of these QSOs to derive accurate systemic redshifts needed to tune the millimetre receivers to the correct frequencies. The near-infrared spectra also provide Hα fluxes and line widths needed to derive reliable BH mass estimates for the QSOs. Our main findings are:

(1) We detect CO emission from six of the ten submm-detected QSOs in our sample, confirming that they contain a significant amount of molecular gas and that a large fraction of the mm emission is from starbursts. The median gas mass of our sample (including non-detections) is $(2.5 \pm 0.7) \times 10^{10}\,{\rm M}_\odot$, similar to that found for $z \sim 2$
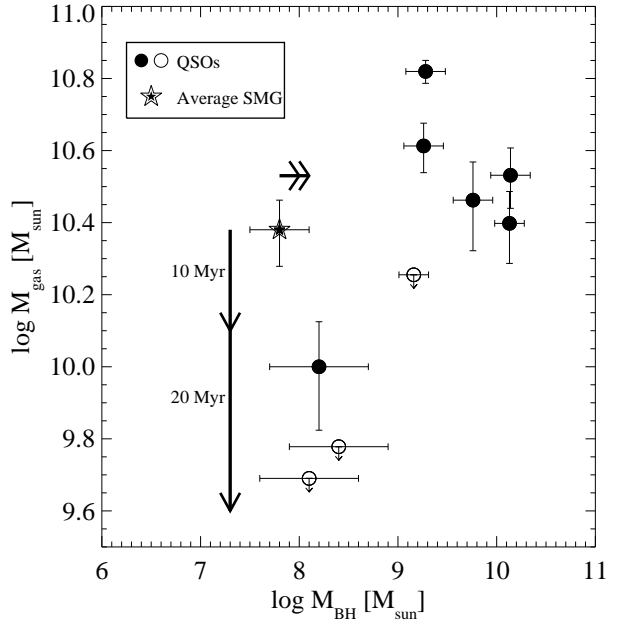

Figure 10. $M_{\rm gas}$ as a function of $M_{\rm BH}$ for our sample of CO-observed submm-detected QSOs. Recall that the quoted errors for $M_{\rm gas}$ do not include the uncertainty on the CO-to-gas conversion factor. The arrows (offset slightly for clarity) indicate the movement of an average SMG in terms of its gas mass depletion and synchronous BH growth in arbitrary scalable timecales of 10 and $20\,{\rm Myr}$, assuming a SFR of $1000\,{\rm M}_\odot\,{\rm yr}^{-1}$ and Eddington-limited BH growth. This demonstrates that an SMG could evolve into $M_{\rm BH} \simeq 10^8\,{\rm M}_\odot$, $M_{\rm gas} \simeq 0.6 \times 10^{10}\,{\rm M}_\odot$ submm-detected QSOs in a reasonable timescale, whereas an average SMG would need substantially ($\sim 10\times$) more gas and more time ($\gtrsim$ SMG lifetime) to evolve into the $M_{\rm BH} \simeq 4 \times 10^9\,{\rm M}_\odot$, $M_{\rm gas} \simeq 3.0 \times 10^{10}\,{\rm M}_\odot$ submm-detected QSOs. This suggests that the submm-detected QSOs hosting BHs of $M_{\rm BH} \simeq 10^8\,{\rm M}_\odot$ with $M_{\rm gas} \lesssim 1 \times 10^{10}\,{\rm M}_\odot$ comprise 'transition objects' that we can use to probe the intermediary evolutionary stage between the SMG and luminous QSO phases, while the rarer more luminous QSOs with $M_{\rm BH} \gtrsim 10^9\,{\rm M}_\odot$ are not related to typical SMGs.

SMGs and to $z \gtrsim 4$ QSOs. The star formation efficiencies of our QSOs are also comparable to those measured for SMGs, $250 \pm 100\,{\rm L}_\odot\,({\rm K\,km\,s}^{-1}\,{\rm pc}^2)^{-1}$, suggesting that the gross properties of the star formation in the QSOs are like those seen in SMGs. Adopting a $2\,{\rm kpc}$ scale size for the gas distribution in the QSOs and a typical inclination of $20°$ we derive a median dynamical mass of ${\rm M}(< 2\,{\rm kpc}) \sim (2.1 \pm 1.4) \times 10^{11}\,{\rm M}_\odot$, similar to SMGs (assuming an inclination angle appropriate for random inclinations). We find a lower incidence of double-peaked CO line profiles in the QSOs, compared to SMGs, which we believe results from a selection bias towards lower average inclination angles for the QSOs.

(2) Our near-infrared spectroscopy indicates a median black hole mass in our QSO sample of $(1.8 \pm 1.3) \times 10^9\,{\rm M}_\odot$. Combined with our dynamical estimates of the spheroid mass, these yield $M_{\rm BH}/M_{\rm sph} \sim 9 \times 10^{-3}$. This $M_{\rm BH}/M_{\rm sph}$ ratio for this sample of submm-detected QSOs at $z = 2$ is an order of magnitude larger than the local ratio, although $M_{\rm sph}$ suffers from large uncertainties due to the unknown

CO radii and inclination angles. This ratio is also significantly above that seen for SMGs at $z \sim 2$. However, this comparison masks a broad range in BH masses within our QSO sample and so we split the sample into two subsets based on their BH masses.

(3) Looking at the optically luminous submm-detected QSOs in our sample we find that we detect CO emission in 5/6 of these QSOs. However, the estimated BH masses for these QSOs, $M_{\mathrm{BH}} \simeq 10^9$–$10^{10}\,\mathrm{M}_\odot$, are too large (and their number densities too small) for them to be related to typical SMGs in a simple evolutionary cycle. We propose that the progenitors of these most massive QSOs are a rare subset of SMGs with $M_{\mathrm{gas}} > 4 \times 10^{11}\,\mathrm{M}_\odot$ with a number density of $\simeq 10\,\mathrm{deg}^{-2}$ which will be possible to detect with future SCUBA-2 surveys.

(4) For the optically less luminous ($\sim L^\star$) submm-detected QSOs, we marginally detect one source in CO and obtain sensitive limits for three further QSOs. The BH masses for these systems are $M_{\mathrm{BH}} \simeq 10^8\,\mathrm{M}_\odot$, similar to the estimates for BHs in SMGs. These submm-detected QSOs are consistent with being 'transition' objects between SMGs and submm-undetected QSOs, as we show it is feasible to link their BH masses to those of SMGs by Eddington limited growth for a period comparable to the gas depletion timescale of the QSOs, ~ 10 Myrs. The space density of these QSOs is also in rough agreement with that expected for the descendents of SMGs given current estimates of the relative lifetimes of QSOs and SMGs. We conclude that these $\sim L^\star$, $M_{\mathrm{BH}} > 10^8\,\mathrm{M}_\odot$ submm-detected QSOs are consistent with being in a very brief prodigious star formation phase, and that they simply do not possess sufficiently large gas reservoirs to sustain the SFR (which is why these might be less often detected in CO), although a larger sample of CO observations of submm-detected QSOs with these BH masses is required for confirmation.

To make further progress on understanding the evolutionary links between SMGs and QSOs requires a larger survey of the submm and CO emission from typical QSOs ($M_{\mathrm{B}} \approx -25$). In addition, measurements of other CO transitions for the submm-detected QSOs (e.g. from IRAM 30-m, ALMA, EVLA, and SKA) are required to place better constraints on the temperature and density of the molecular gas and thus provide a more accurate determination of the line luminosity ratios and hence total gas masses of these systems. Similarly, higher resolution CO observations are essential to put strong constraints on the reservoir sizes and inclination angles, and hence M_{dyn}, needed to compare the two populations. Finally, better measurements of the far-infrared SEDs (with SABOCA, SCUBA-2 or *Herschel*) will yield more accurate measures of L_{FIR} and T_{dust} for submm-detected QSOs to constrain the contribution from an AGN component.

REFERENCES

Alexander D.M. et al., 2003, AJ, 125, 383

Alexander D.M., Smail I., Bauer F.E., Chapman S.C., Blain A.W., Brandt W.N., Ivison R.J., 2005a, Nat., 434, 738

Alexander D.M., Bauer F.E., Chapman S.C., Smail I., Blain A.W., Brandt W.N., Ivison R.J., 2005b, ApJ, 632, 736

Alexander D.M. et al., 2008, AJ, 135, 1968

Avni Y., Soltan A., Tananbaum H., Zamorani G., 1980, ApJ, 238, 800

Beelen A. et al., 2004, A&A, 423, 441

Beelen A., Cox P., Benford D., Dowell C.D., Kovács A., Bertoldi F., Omont A., Carilli C.L., 2006, ApJ, 642, 694

Bell E.F. et al., 2004, ApJ, 608, 752

Biggs A.D., Ivison R.J., 2006, MNRAS, 371, 963

Bonning E.W., Shields G.A., Salviander S., McLure R.J., 2005, ApJ, 626, 89

Borys C., Smail I., Chapman S.C., Blain A.W., Alexander D.M., Ivison R.J., 2005, ApJ, 635, 853

Bower R.G., Benson A.J., Malbon R., Helly J.C., Frenk C.S., Baugh C.M., Cole S., Lacey C.G., 2006, MNRAS, 370, 645

Boyle B.J., Shanks T., Croom S.M., Smith R.J., Miller L., Loaring N., Heymans C., 2000, MNRAS, 317, 1014

Calzetti D., Armus L., Bohlin R.C., Kinney A.L., Koornneef J., Storchi-Bergmann T., 2000, ApJ, 533, 682

Carilli C.L., Wang R., 2006, AJ, 131, 2763

Cavanagh B., Hirst P., Jenness T., Economou F., Currie M.J., Todd S., Ryder S.D., 2003, in Payne H.E., Jedrzejewski R.I., Hook R.N., eds, ASP Conf. Ser. Vol. 295, Astronomical Data Analysis Software and Systems XII, p. 237

Chapman S.C., Blain A.W., Ivison R.J., Smail I.R., 2003, Nat., 422, 695

Chapman S.C., Blain A.W., Smail I., Ivison R.J., 2005, ApJ, 622, 772

Coppin K., et al., 2006, MNRAS, 372, 1621

Coppin K., et al., 2008, MNRAS, 384, 1597

Di Matteo T., Springel V., Hernquist L., 2005, Nat., 433, 604

Downes D., Solomon P.M., 1998, ApJ, 507, 615

Fan X. et al., 1999, AJ, 118, 1

Fan X. et al., 2001, AJ, 122, 2833

Feigelson E.D., Nelson P.I., 1985, ApJ, 293, 192

Frayer D. T., Ivison R.J., Scoville N.Z., Yun M., Evans A.S., Smail I., Blain A. W., Kneib J.-P., 1998, ApJ, 506, L7

Gebhardt K. et al., 2000, ApJ, 539, 13

Genzel R., Baker A.J., Tacconi L.J., Lutz D., Cox P., Guilloteau S., Omont A., 2003, ApJ, 584, 633

Goncalves T.S., Steidel C.C., Pettini M., 2008, ApJ, 676, 816

Greene J.E., Ho L.C., 2005, ApJ, 630, 122

Greve T.R., Ivison R.J., Bertoldi F., Stevens J.A., Dunlop J.S., Lutz D., Carilli C.L., 2004, MNRAS, 354, 779

Greve T.R. et al., 2005, MNRAS, 359, 1165

Greve T.R., Hainline L.J., Blain A.W., Smail I., Ivison R.J., Papadopoulos P.P., 2006, AJ, 132, 1938

Guilloteau S., Omont A., Cox P., McMahon R.G., Petitjean P., 1999, A&A, 349, 363

Guilloteau S., Lucas R., 2000, in Mangum J.G., Radford S.J.E., eds, ASP Conf. Ser. Vol. 217, Imaging at Radio through Submillimeter Wavelengths, p. 299

Hainline L.J., Scoville N.Z., Yun M.S., Hawkins D.W., Frayer D.T., Isaak K.G., 2004, ApJ, 609, 61

Häring N., Rix H.-W., 2004, ApJ, 604, L89

Hopkins P.F., Hernquist L., Cox T.J., Di Matteo T., Martini P., Robertson B., Springel V., 2005, ApJ, 630, 705

Humphrey P. J., Buote D. A., Brighenti F., Gebhardt K., Mathews W. G., 2008, preprint(astro-ph/0801.3461)

Ivison R.J., et al., 2007, MNRAS, 380, 199

Kennicutt R.C., 1998, ARA&A, 36, 189

Kovács A., Chapman S.C., Dowell C.D., Blain A.W., Ivison R.J., Smail I., Phillips T.G., 2006, ApJ, 650, 592

Krips M., Eckart A., Neri R., Bertram T., Straubmeier C, Fischer S., Staguhn J.G., Vogel S.N., A&A, 464, 187

Lutz D. et al., 2007, ApJ, 661, L25

Macchetto F., Marconi A., Axon D. J., Capetti A., Sparks W., Crane P., 1997, ApJ, 489, 579

Magorrian J. et al., 1998, AJ, 115, 2285

Maiolino R. et al., 2007, A&A, 472, L33

Marconi A., Hunt L.K., 2003, ApJ, 589, 21

Martini P., Weinberg D.H., 2001, ApJ, 547, 12

McLure R.J., Dunlop J.S., 2004, MNRAS, 352, 1390

McLure R.J., Jarvis M.J., Targett T.A., Dunlop J.S., Best P.N., 2006, MNRAS, 368, 1395

Nelson C.H., 2000, ApJ, 544, L91

Nelson C.H., Whittle M., 1996, ApJ, 465, 96

Omont, A., McMahon R.G., Cox P., Kreysa E., Bergeron J., Pajot F., Storrie-Lombardi L.J., 1996, A&A, 315, 1

Omont, A., Cox P., Bertoldi F., McMahon R.G., Carilli C., Isaak K.G., 2001, A&A, 374, 371

Omont, A., Beelen, A., Bertoldi F., Cox P., Carilli C.L., Priddey R.S., McMahon R.G., Isaak K.G., 2003, A&A, 398, 857

Page M.J., Stevens J.A., Mittaz J.P.D., Carrera F.J., 2001, Sci, 294, 2516

Page M.J., Stevens J.A., Ivison R.J., Carrera F.J., 2004, ApJ, 611, L85

Peng C.Y., Impey C.D., Ho L.C., Barton E.J., Rix H.-W., 2006, ApJ, 640, 114

Petric A.O., Carilli C.L., Bertoldi F., Beelen A., Cox P., Omont A., 2006, AJ, 132, 1307

Ramsay Howat S.K. et al., 2004, in Moorwood A.F.M., Masanori I., eds, SPIE Conf. Proc. Vol. 5492, Ground-based Instrumentation for Astronomy, p. 1160

Riechers D.A. et al., 2006, ApJ, 650, 604

Riechers D.A., Walter F., Brewer B.J., Carilli C.L., Lewis G.F., Bertoldi F., Cox P., 2008, preprint(astro-ph/0806.4616)

Salpeter E.E., 1955, 121, 161

Sanders D.B., Soifer B.T., Elias J.H., Neugebauer G., Matthews K., 1988, ApJ, 328, L35

Sanders D.B., Scoville N.Z., Soifer B.T., 1991, ApJ, 370, 158

Seaquist E.R., Ivison R.J., Hall P.J., 1995, MNRAS, 276, 867

Shields G.A., Menezes K.L., Massart C.A., Vanden Bout P., 2006, ApJ, 641, 683

Smail I., Ivison R.J., Blain A.W., 1997, ApJL, 490, L5

Smail I., Chapman S.C., Blain A.W., Ivison R.J., 2004, ApJ, 616, 71

Stevens J.A., Page M.J., Ivison R.J., Smail I., Carrera F.J., 2004, ApJ, 604, L17

Stevens J.A., Page M.J., Ivison R.J., Carrera F.J., Mittaz J.P.D., Smail I., McHardy I.M., 2005, MNRAS, 360, 610

Solomon P.M., Downes D., Radford S.J.E., Barrett J.W., 1997, ApJ, 478, 144

Solomon P.M., Vanden Bout P.A., 2005, ARA&A, 43, 677

Spergel D.N. et al., 2003, ApJS, 148, 175

Staguhn J.G., Schinnerer E., Eckart A., Scharwächter J., 2004, ApJ, 609, 85

Swinbank, A. M., Smail, I., Chapman, S. C., Blain, A. W., Ivison, R. J., Keel, W. C., 2004, ApJ, 617, 64

Swinbank A. M. et al., 2005, MNRAS, 359, 401

Swinbank, A. M., Chapman, S. C., Smail, I., Lindner, C., Borys, C., Blain, A. W., Ivison R. J., Lewis, G. F., 2006, MNRAS, 371, 465

Tacconi L.J., Genzel R., Lutz D., Rigopoulou D., Baker A.J., Iserlohe C., Tecza M., 2002, ApJ, 580, 73

Tacconi L.J. et al., 2006, ApJ, 640, 228

Tacconi L.J. et al., 2008, ApJ, 680, 246

Takata T., Sekiguchi K., Smail I., Chapman S.C., Geach J.E., Swinbank A.M., Blain A., Ivison R.J., 2006, ApJ, 651, 713

Valtonen M. J., et al. 2007, American Astronomical Society Meeting Abstracts, 211, #112.07

Wall J.V., Jenkins C.R., 2003, Practical Statistics for Astronomers. Cambridge Univ. Press, Cambridge

Walter F., Carilli C., Bertoldi F., Menten K., Cox P., Lo K.Y., Fan X., Strauss M.A., 2004, ApJ, 615, L17

Wang R. et al., 2007, AJ, 134, 617

Wang R. et al., 2008, AJ, 135, 1201

Weiss A., Downes D., Neri R., Walter F., Henkel C., Wilder D.J., Wagg J., Wiklind T., 2007, A&A, 467, 955

Wright E.L., 2006, PASP, 118, 1711

Yao L., Seaquist E.R., Kuno N., Dunne L., 2003, ApJ, 588, 771